Doppler lidar mounted on a wind turbine nacelle – UPWIND deliverable D6.7.1

Angelou, Nikolas; Mann, Jakob; Courtney, Michael; Sjöholm, Mikael

Publication date:
2010

Document Version
Publisher's PDF, also known as Version of record

Doppler lidar mounted on a wind turbine nacelle – UPWIND deliverable D6.7.1

Risø-R-Report

Nikolas Angelou, Jakob Mann, Mike Courtney, Mikael Sjöholm
Risø-R-1757(EN)
December 2010

Risø DTU
National Laboratory for Sustainable Energy

Author: Nikolas Angelou, Jakob Mann, Mike Courtney, Mikael Sjöholm
Title: Doppler lidar mounted on a wind turbine nacelle – UPWIND deliverable D6.7.1
Division: Wind Energy

Risø-R-1757 (EN)
December 2010

Abstract (max. 2000 char.):

A ZephIR prototype wind lidar manufactured by QinetiQ was mounted on the nacelle of a Vestas V27 wind turbine and measurements of the incoming wind flow towards the rotor of the wind turbine were acquired for approximately 3 months (April - June 2009). The objective of this experiment was the investigation of the turbulence attenuation induced in the lidar measurements.

In this report are presented results from data analysis over a 21-hour period (2009-05-05 12:00 – 2009-05-06 09:00). During this period the wind turbine was not operating and the line-of-sight of the lidar was aligned with the wind direction.

The analysis included a correlation study between the ZephIR lidar and a METEK sonic anemometer. The correlation analysis was performed using both 10 minutes and 10 Hz wind speed values.

The spectral transfer function which describes the turbulence attenuation, which is induced in the lidar measurements, was estimated by means of spectral analysis.

An attempt to increase the resolution of the wind speed measurements of a cw lidar was performed, through the deconvolution of the lidar signal. A theoretical model of such a procedure is presented in this report. A simulation has validated the capability of the algorithm to deconvolve and consequently increase the resolution of the lidar system. However the proposed method was not efficient when applied to real lidar wind speed measurements, probably due to the effect, that the wind direction fluctuations along the lidar's line-of-sight have, on the lidar measurements.

ISSN 0106-2840
ISBN 978-87-550-3868-4

Contract no.:

Group's own reg. no.:
(Føniks PSP-element)

Sponsorship:

Cover : ZephIR prototype optical head mounted on the nacelle of the V27 wind turbine

Pages: 43
Tables: 6
References: 18

Information Service Department
Risø National Laboratory for Sustainable Energy
Technical University of Denmark
P.O.Box 49
DK-4000 Roskilde
Denmark
Telephone +45 46774005
bibl@risoe.dtu.dk
Fax +45 46774013
www.risoe.dtu.dk

Nomenclature

λ	Emission wavelength [nm]
v	Wind speed [$\mathrm{m\,s^{-1}}$]
v_r	Radial wind speed [$\mathrm{m\,s^{-1}}$]
v_s	Sonic wind speed measurement projected in the lidar's line-of-sight [$\mathrm{m\,s^{-1}}$]
φ	Spatial Weighting function
a_o	Effective radius of the lidar's telescope [mm]
k	Wavenumber [$\mathrm{m^{-1}}$]
r	Focus distance [m]
R^2	Coefficient of determination
R_u	Covariance
S	Power spectral density
s	Distance from the lidar's focal point [m]
W	Window function
X	Cross spectrum
z_R	Rayleigh length [m]

Contents

1 Introduction

The applications of remote sensing techniques in wind observations offer a great potential to the accurate study of the wind and they can be considered as an important tool for the further evolution of wind energy research. In specific, a Doppler wind LIght Detection And Ranging (lidar) system is capable of providing remote sensing measurements of the wind characteristics (speed, turbulence and direction). The advantages of this technique have been documented and presented in [1].

One important aim in the wind energy research is the development of methods for the characterization of the incoming wind flow towards the rotor of the wind turbine. Upwind measurements can lead both to the increase of the wind turbine's life time (detection of extreme wind events, e.g. wind gusts) and to the improvement of its power production (rpm, pitch and yaw control). Additionally, the knowledge of the exact wind which is flowing towards the wind turbine rotor can improve the accuracy of the power performance analysis [2]. Nowadays the lidar instruments are offering the flexibility of being mounted on a wind turbine nacelle, and thus providing wind measurements in various distances away from the wind turbine's rotor. A detailed description of the technological requirements for such an application is documented in [3] and the feasibility of this concept was demonstrated in an experiment in 2003, where a lidar mounted on a turbine's nacelle was used for the detection of wind gusts [4]. Recent advancements of such applications, include the calculation of the yaw misalignment of the wind turbine using wind lidar systems, which are either installed in the rotating spinner [5] or mounted on top of the nacelle of a wind turbine [6].

In this study a ZephIR prototype lidar manufactured by QinetiQ (UK) was mounted on the top of the nacelle of a Vestas V27 wind turbine. The performance of this lidar instrument has been previously tested and it has proven capable of providing accurate wind speed measurements [7][8]. The experiment took place from the middle of April 2009 until the end of August 2009. The objectives of this experiment were: a) the study of the properties of the lidar wind speed measurements (spatial filtering and deconvolution of the lidar signal), b) the investigation of the incoming wind field (pressure stagnation and Taylor's Frozen turbulence theory) and c) the wind turbine's power curve analysis using lidar radial wind speed measurements.

Due to technical issues concerning the operation of the ZephIR prototype lidar, only approximately one month of data are presumed to be trustworthy. Due to this limited data availability, the analysis was concentrated on the first objective of the experiment which was the properties of the lidar measurements. In particular, the spectral transfer function, which indicates the attenuation of the wind turbulence in the lidar measurements was investigated. Furthermore a method based on a deconvolution of the lidar signal was applied, aiming at increasing the resolution of the measurements.

Additionally the lidar data were used in order to investigate the impact of the wind speed fluctuations in the wind turbine power production [9].

2 Experiment Description

During the experiment a ZephIR prototype lidar was mounted on the nacelle of a V27 wind turbine, which is installed inside the Risø DTU site area (55°41′08″ N, 12°05′46″ E). The V27 wind turbine is a 225 kW model, with a hub height of 33.5 m and a rotor diameter equal to 27 m. Figure 1 shows a satellite picture (Google Earth©) of the area where the V27 wind turbine (#1 in Figure 1) is placed. In the adjacent area three other wind turbines can be found. Two of them are in the direction 195° South - South West

from the V27 wind turbine at distances of 120 m and 190 m, respectively. While the third one is found in the direction 15° North at a distance of approximately 80 m. A met mast (M in Figure 1) has been placed in the direction of 283° N at a distance of approximately 67.5 m (equivalent with 2.5 rotor diameters) from the V27 wind turbine. West from the V27 wind turbine is the Roskilde Fjord, and to the east is the mainland. The terrain is covered with low vegetation (crop fields) and can be assumed to be in general flat.

Figure 1: Satellite picture of the Risø site area (Google Earth©).

2.1 Meteorological mast (met mast)

The met mast was equipped with sonic and cup anemometers, as well as with wind vanes, measuring the speed and direction of the wind. The data from the met mast instruments were acquired at 32 Hz. Table 1 contains the details regarding the instrumentation installed at the met mast.

Height [m]	**Instrument**
45	METEK 3D sonic anemometer, cup anemometer (P2546A)
32	METEK 3D sonic anemometer, cup anemometer (P2546A)
30	2 cup anemometers (P2546A), W200P wind vane, HMP45A RH (Relative Humidity), T-Probe
18	METEK 3D sonic anemometer, cup anemometer (P2546A)
2	Precipitation monitor

Table 1: Meteorological mast instrumentation

2.2 ZephIR prototype wind lidar

The ZephIR prototype is a continuous wave wind lidar capable of acquiring fast measurements at different distances from the instrument. It is designed to operate in a staring or a conical mode, the latter being achieved through the deflection of the laser beam by a rotating optical wedge prism. The wavelength of emission is 1547 nm and the maximum output power is 1 W. The ZephIR prototype consists of two parts, an optical head and an optoelectronic unit. The optical head contains the telescope from which the laser beam is transmitted and received. The optoelectronic unit is separated in an emission part (laser and amplifier) and a detector of the backscattered signal and is connected through a fiber cable to the optical head. The setup with a fiber cable provides flexibility as far as it concerns the applications in which it is used. Hence it was feasible to install the optical head of the lidar on top of the wind turbine's nacelle (see Figure 2) with the optoelectronics rack placed in the base of the tower. The theoretical resolution (both temporal and spatial) of this lidar system is presented in [10].

Figure 2: ZephIR lidar's optical head mounted on the V27 wind turbine's nacelle

2.2.1 Operation parameters

Throughout the whole period of the experiment, the lidar was operating in a staring mode. The focus distance of the laser beam was set to 67.5 m, which is approximately equal with the horizontal distance between the V27 wind turbine and the met mast (see Figure 1). The ZephIR prototype data acquisition unit (DAU) had a sampling rate of 50 MHz. A Fast Fourier Transformation (FFT) was applied in sequences of 512 consecutive measurements in order to create power density spectra of the wind speed fluctuations. These spectra contain information regarding the Doppler shift of the frequency of the emitted radiation, which is induced by the relative motion of the atmospheric aerosols. Approximately 97656 ($50 \times 10^6/512$) of these spectra were created per second. In order to achieve adequate values of Carrier-To-Noise ratio (CNR) 1952 power density spectra were averaged, resulting in a data stream of approximately 50 Doppler spectra per second. An on-line access to the instrument's configuration system was established through an Ethernet connection to the computer of the lidar.

Wavelength [nm]	1547.615
Power [W]	0.85
DAU sampling rate [MHz]	50
Diameter of the optical lens [cm]	7.62
Spectra per second [Hz]	~ 50
Focus distance [m]	67.5
Spectrum bandwidth [MHz]	25
Frequency resolution [MHz/bin]	0.0976563

Table 2: ZephIR prototype lidar's (Gray unit)operation parameters.

2.2.2 Wind speed calculation

Each Doppler spectrum streamed from the ZephIR is represented in 256 bins in a bandwidth of 25 MHz. The first bin represents the 0 $\mathrm{m\,s^{-1}}$. The frequency resolution of each of the spectrum is defined as:

$$\text{Frequency resolution} = \frac{\text{Bandwidth}}{\text{Number of bins}} = \frac{25\ \text{MHz}}{256\ bin} = 0.0976563\ \text{MHz}/bin \qquad (1)$$

The Doppler spectra produced by the FFT were post processed in order to filter out the relative-intensity-noise (RIN) produced by the laser. Additionally, it was necessary to calculate a threshold parameter for each individual spectrum. The threshold indicated the level of background noise induced to the detector during the detection of an atmospheric backscattered signal. This level was calculated and consequently subtracted from each spectrum. A median frequency method was used to detect the characteristic frequency of the Doppler shift of each filtered spectrum.

The wind speed can be calculated based on the Doppler theory, according to which the frequency shift is proportional to the ratio between the wind speed and the propagation speed of the laser light:

$$\frac{\Delta f}{f} = \frac{2\upsilon}{c} \Longrightarrow \upsilon = \frac{1}{2}\lambda\Delta f = \frac{1}{2}\lambda \cdot (0.0976563 \times 10^6 \cdot bin)\ \mathrm{s^{-1}} \qquad (2)$$

Where Δf is the Doppler shift, c is the speed of the light, υ is the wind speed, λ is the wavelength of the emitted laser radiation and *bin* the bin number that represents the Doppler shift frequency. In the case of the ZephIR prototype (Gray unit) the wavelength of the emitted light is equal to 1547.615 nm, hence the equation (2) becomes:

$$\upsilon = \frac{1}{2}(1547.615 \times 10^{-9}\mathrm{m})(0.0976563 \times 10^6 \cdot bin)\ \mathrm{s^{-1}} = 0.075 \cdot bin\ \mathrm{m\,s^{-1}} \qquad (3)$$

2.2.3 Convolution of the lidar signal

One of the parameters that describes the laser beam of the lidar is the probe length. In the case of a cw lidar this is defined as twice the Rayleigh length (z_R)[1], which is equal to [11]:

$$z_R = \frac{\lambda}{\pi}\frac{r^2}{a_o^2} \tag{4}$$

Where λ is the wavelength of the emitted radiation, r the distance between the telescope of the lidar and the point where the laser beam is focused (focus distance) and a_o is the effective radius of the telescope used for emitting and receiving the laser signal. The effective radius can be defined as the radius where the intensity has dropped to e^{-2} of its maximum value. In the case of the ZephIR prototype the a_o is expected to be equal to 24 mm [12], and the equation (4) can be written as $z_R \approx 0.00085 \cdot r^2$.

Due to the fact that the laser beam is characterized by a probe length, the lidar wind speed measurements should not be considered as point measurements but rather as weighted averages of various speeds which are contained in a certain volume of air. The size of the sampling volume is dependent on the probe length and consequently to the focus distance. The further the distance where the lidar is focused the larger the scanned volume is. This has been studied by [13] where it is proposed that the radial wind speed $\upsilon_r(x)$ measurement can be assumed to be equal with the integral:

$$\upsilon_r(x) = \int_{-\infty}^{\infty} \varphi(s)\mathbf{n} \cdot u(s\mathbf{n} + x)ds \tag{5}$$

Where $\mathbf{n}$ is a unity vector in the line-of-sight of the lidar, x is the center of the probe volume, s is a distance along the line-of-sight from x, u the wind field (in this study it is expected that the main wind vector is in the horizontal plane) and $\varphi(s)$ is a Lorentzian function. In the case of a cw lidar this can be defined as [14]:

$$\varphi(s) = \frac{1}{\pi}\frac{z_R}{z_R^2 + s^2} \tag{6}$$

Figure 3 presents the spatial weighting function for two different formulas of the Rayleigh length (z_R). The first corresponds to the equation (4) (a_o= 24 mm, red solid line) and the second proposed by [12], where it was observed less beam divergence from the optical fiber end (a_o= 19.5 mm, red dashed line), thus smaller effective area a_o and consequently larger values of the z_R:

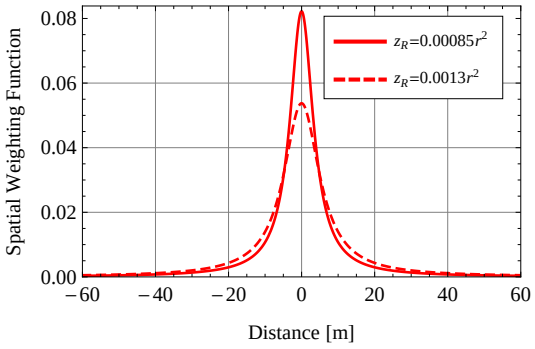

Figure 3: Spatial Weighting Function for two Rayleigh length formulas.

[1]The Rayleigh length is the distance, along the line-of-sight of the lidar, between the laser beam's waist and the position where the area of the cross section is doubled.

The averaging of the radial wind speeds due to the spatial weighting function will have a similar effect as a low-pass filter. Consequently it is expected that very fast fluctuations of the wind speed will be filtered out from the lidar radial wind speed measurements. This expression of the lidar's wind speed measurement $v_r(x)$ (see equation (5)) is based on the assumption that the aerosols in the probe volume are homogeneously distributed [15].

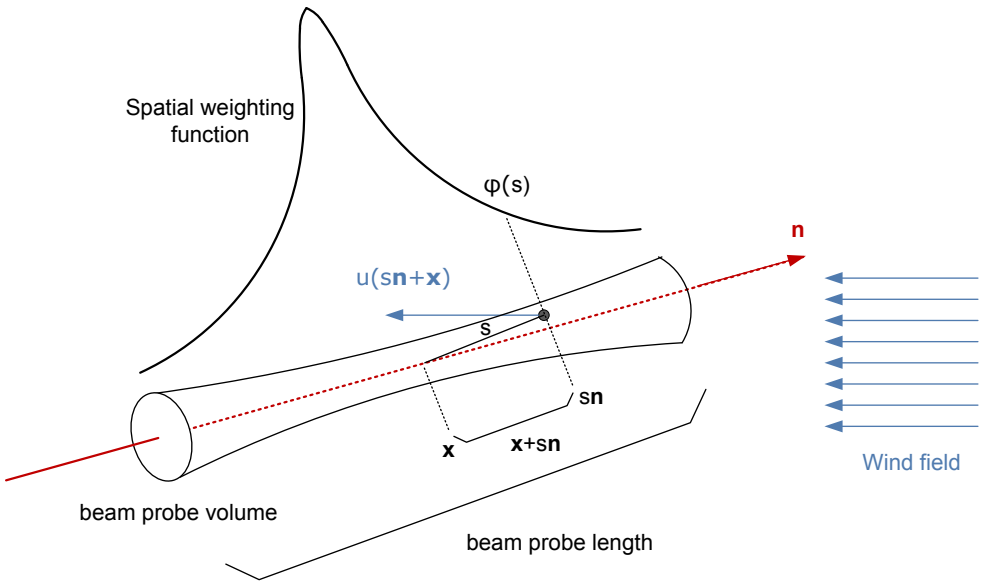

Figure 4: Representation of the spatial averaging effect of the measurement of a cw lidar.

2.3 Data overview

The ZephIR prototype lidar was mounted on the V27 wind turbine on the 2009-04-16, and the measurement campaign lasted until the 2009-08-26. Approximately 1757 hours (∼73 days) of data were acquired during the whole period of the experiment. Table 3 contains details regarding the periods where lidar data were acquired. In the last column the availability of data for each period is presented. The availability of the data was expected to be around ∼94.5%, because the ZephIR lidar was not streaming data for a 10-min period every 3 hours. This was observed due to the fact that every 3 hours, a series of measurements were acquired from the ZephIR prototype with the laser's shutter closed, in order to calculate the RIN spectrum.

Period [#]	**Date**	**Data**[#]	[%]
1	2009/04/17 13:40 - 2009/04/27 14:10	1335	92.5%
2	2009/05/05 09:20 - 2009/05/21 13:10	2134	92.0%
3	2009/06/03 09:30 - 2009/06/17 16:10	1872	91.1%
4	2009/07/16 10:00 - 2009/07/20 08:10	501	88.7%
5	2009/07/23 10:50 - 2009/08/03 08:40	1395	88.8%
6	2009/08/06 10:30 - 2009/08/26 13:30	2702	93.0%

Table 3: Periods regarding data availability.

On the 2009-06-01 the performance of the lidar appeared to degrade, which can be seen in figure 6 that presents the time series of the scaling factors values, since the scaling factor is a parameter that indicates the sensitivity of the lidar. It is observed that from 2009-06-01 and until the end of the campaign, the scaling factor values were gradually increasing, indicating a decrease in the signal strength. The operation of the lidar was evaluated after the end of the experiment and the drop of the sensitivity was attributed to malfunctions both in the power cables connection and in the detection of the lidar signals.

Due to this fact only data acquired during the periods 2009-04-16 - 2009-04-27 and 2009-05-05 - 2009-05-21 can be considered reliable. In these time intervals 3662 data files were collected, which correspond to 610 hours and is equal to the 34.7% of the total amount of data.

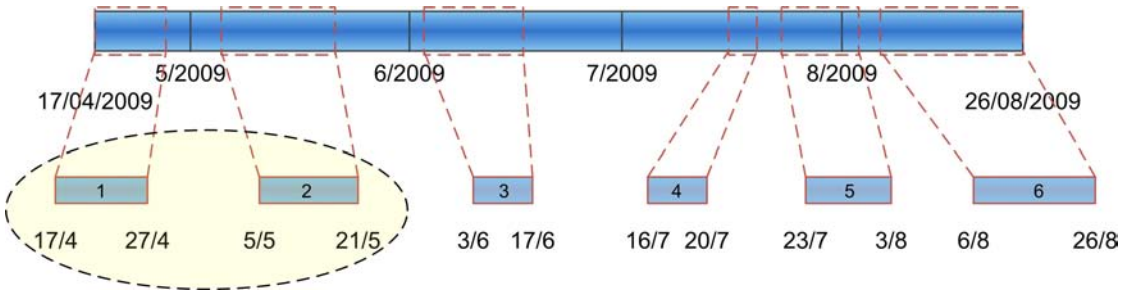

Figure 5: Period of the measurement campaign.

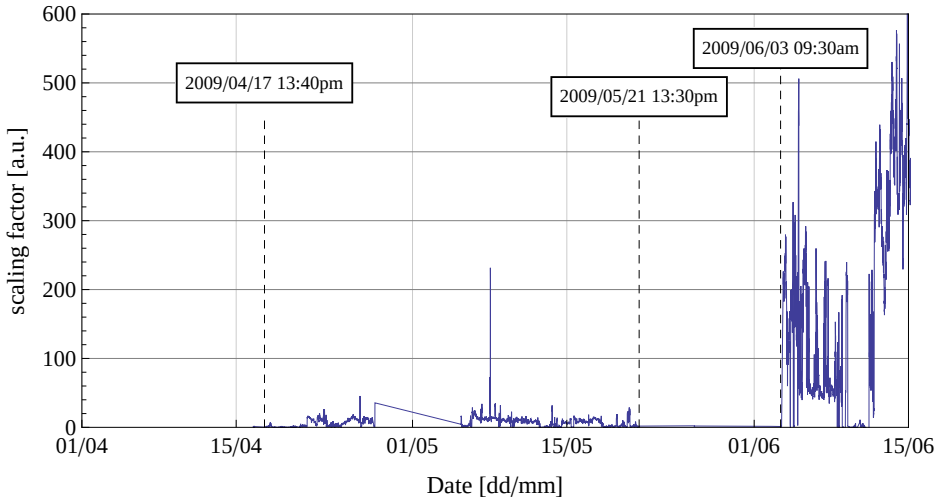

Figure 6: Time series of the scaling factor of the ZephIR prototype lidar (2009-05-05 - 2009-06-15).

3 Case study

The analysis presented in this section is based on the data which were acquired between the 2009-05-05 12:00 and the 2009-05-06 09:00. The objective was to acquire radial wind speed measurements looking upwind towards the met mast, while the wind direction coincided the line-of-sight of the lidar. The wind turbine was yawed and its orientation was locked in the direction of 283°, which is the relative direction of the met mast in reference with the location of the V27 wind turbine. Throughout this period the wind turbine was not operating, thus achieving maximum lidar data availability, due to the fact that the wind turbine's blades were not blocking the lidar beam. The vector **n** of the line-of-sight of the lidar was pointing approximately one meter above the sonic anemometer of the met mast (placed at a height of 32 m, #1 in Figure 7). The aim of the analysis was to investigate the turbulence attenuation at high frequencies induced by the sampling volume of the lidar.

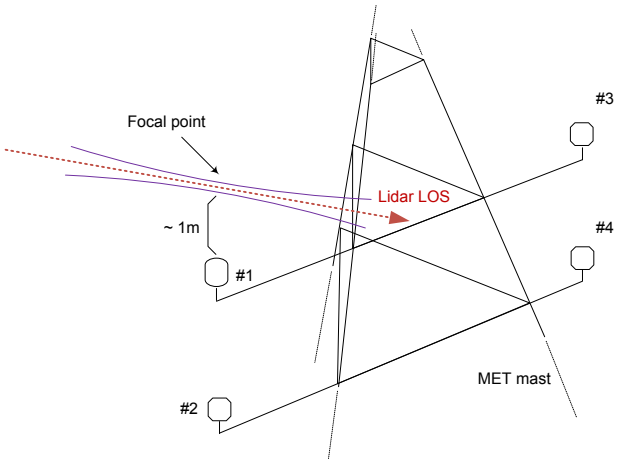

Figure 7: Schematics of the focus position of the laser beam in reference with the structure of the met mast (#1 sonic and #2 cup anemometer at a height of 32 m, #3 and #4 cup anemometers at 30 m).

3.1 Wind characteristics

During the selected period of investigation the direction and the speed of the wind were measured by a METEK sonic anemometer installed in the met mast at height of 32 m. The wind direction was observed to vary from 300° to 160° (see Figure 8), while the wind speed varied between 6 $\mathrm{m\,s^{-1}}$ and 14 $\mathrm{m\,s^{-1}}$ (see Figure 9, purple line).

During the 4 hours (2009-05-05 12:00 - 18:00) of the period the wind direction could be found around 280° and 290° while wind speeds between 8 and 12 $\mathrm{m\,s^{-1}}$ were observed. Subsequently, in the next 9 hours a counter-clockwise drift of the wind direction from 280° to 160° was observed, accompanied with a drop in the wind speed reaching the lowest speed of almost 2.5 $\mathrm{m\,s^{-1}}$. In the last 6 hours of the period the wind turned again moving from 160° to 240° with an increasing wind speed from 2.5 $\mathrm{ms^{-1}}$ to 10 $\mathrm{m\,s^{-1}}$. Due to the fact that the wind turbine yaw was locked throughout this time period, the lidar was not looking all the time towards the wind direction. Thus the angle between the wind flow and the LOS of the lidar was increasing and thus the projection of the wind

speed to the LOS was decreasing. This had as a result that the lidar was measuring lower wind speeds than the sonic anemometer (see Figure 9, blue line).

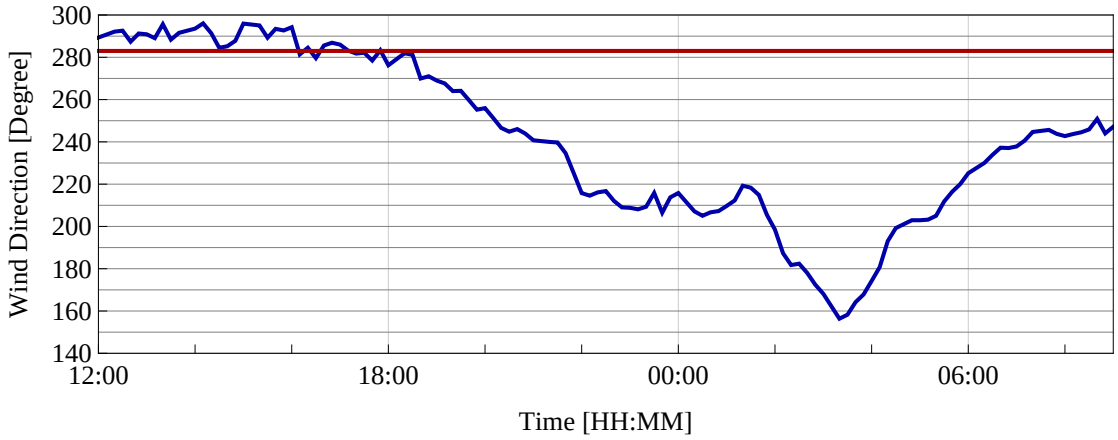

Figure 8: Wind direction (blue) as measured from a sonic anemometer at 32 m and yaw direction of the wind turbine (red) during the period between 2009-05-05 12:00 - 2009-05-06 09:00.

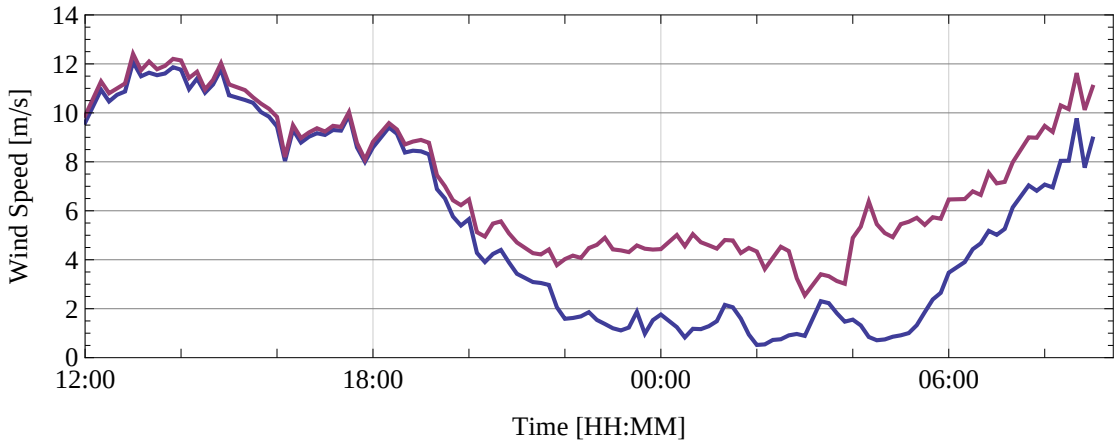

Figure 9: Wind speed as measured from a sonic anemometer (purple) and a lidar (blue) at 32 m during the period between 2009-05-05 12:00 - 2009-05-06 09:00.

3.2 Lidar - sonic anemometer correlation

In order to perform a correlation analysis between the lidar and the sonic, it was necessary to project the wind speed measurements from the sonic anemometer to the line-of-sight (**n**) of the lidar. The projection was done in the x-y plane, using the sonic measurements in the x and y axis, u_x and u_y respectively. The projection is described by the equation:

$$v_s = |u_x \cos\theta + u_y \sin\theta| \tag{7}$$

Where θ is the relative angle between the orientation of the axis of the sonic anemometer and the line-of-sight of the lidar (see Figure 10).

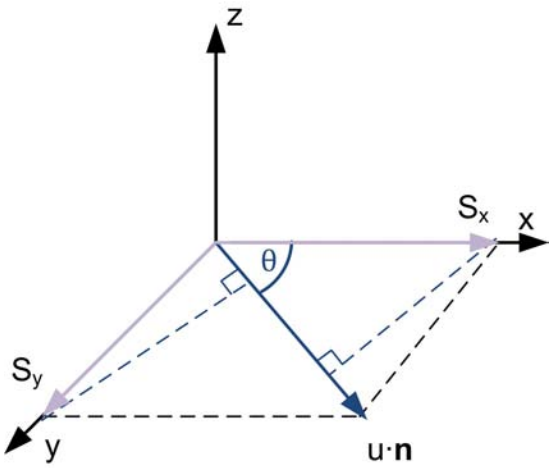

Figure 10: Wind Speed Projection.

The cross correlation between the 10-minutes mean values of the lidar measured radial wind speed (v_r) and the projection of the sonic measurements to the line-of-sight of the lidar (v_s) was calculated for a running step of 0.5° of the relative angle θ. The maximum correlation appeared for θ values equal to 93.5° (see Figure 11).

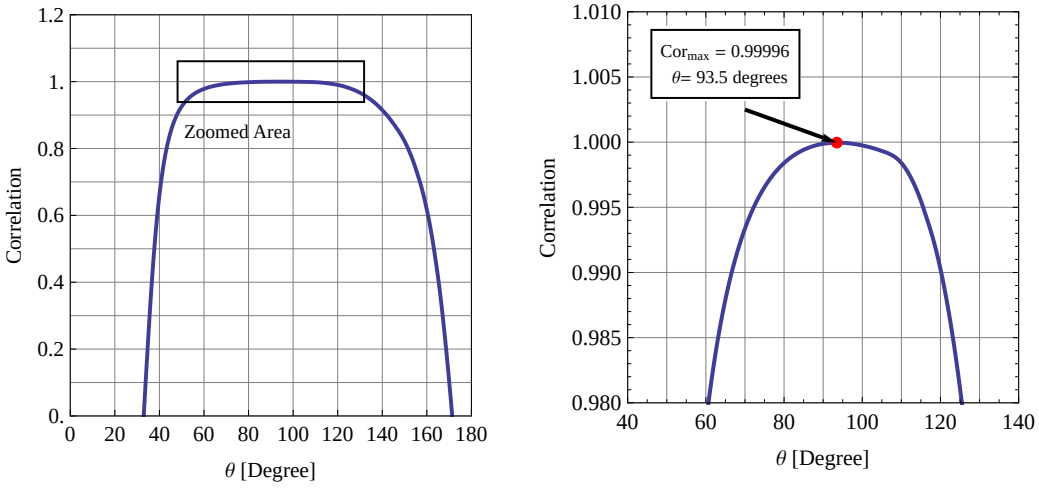

(a) (b)

Figure 11: Lidar sonic correlation in the horizontal plane.

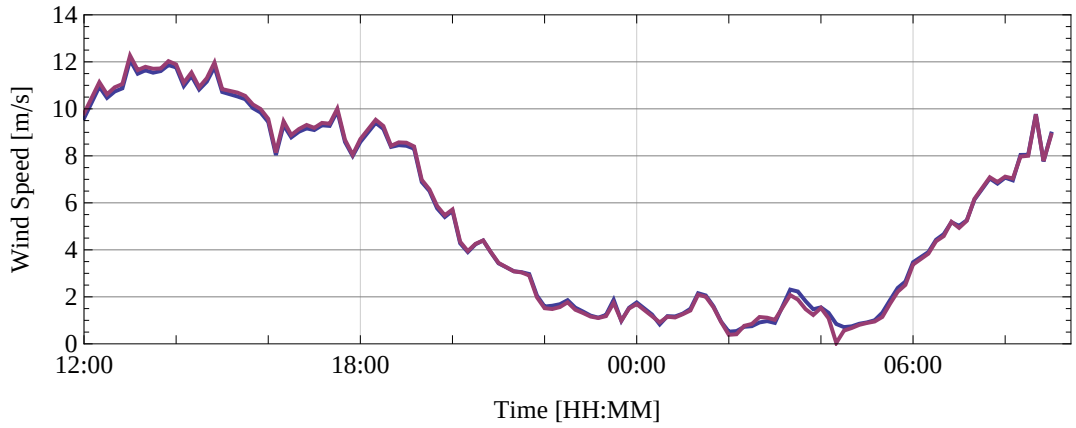

Figure 12: Projected wind speed as measured from a sonic anemometer (purple) and a lidar (blue) at 32 m during the period between 2009-05-05 12:00 and 2009-05-06 09:00.

Figure 12 presents the 10-min mean values of the lidar radial wind speed measurements (blue line), along with the sonic measurements projected to the line-of-sight of the lidar. In general a high correlation between the two time series can be observed (see Figure 13, left). The correlation coefficient (R^2) was calculated to be equal to 0.9993, while a linear fit to the data indicated an offset of 0.116 ms^{-1} between the lidar and the sonic measurements. The correlation analysis was repeated by taking into account only the 10-min average values that were larger than 2 ms^{-1}, in order to exclude the data sets where the lidar was approaching the limits of the minimum detectable wind speed. However there is not observed any change in the correlation (see Figure 13, right).

From the regression analysis between the sonic anemometer and lidar wind speed measurements an underestimation equal to 2.4% and 2.7%, for the two different data sets, is observed. This can be attributed to the fact the Metek sonic anemometer is USA-1 type, which corrects the flow distortion in a more rudimentary way than the USA-1 scientific type.

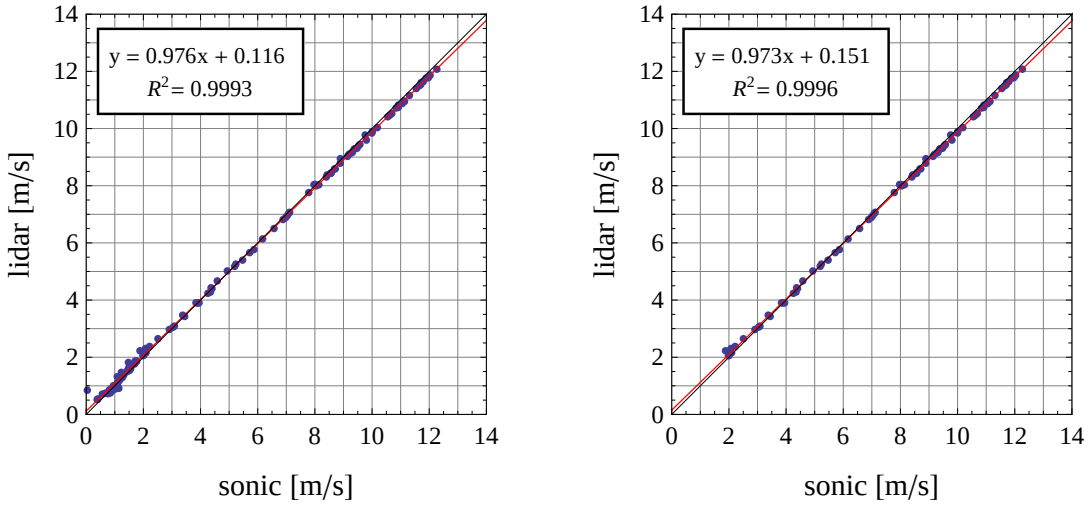

(a) (b)

Figure 13: Lidar - Sonic correlation analysis using 10-min mean values (Left: all the data, Right: only $v \geq 2$ ms^{-1}).

3.2.1 Time periods

In order to investigate the effect of the convolution of the spatial weighting function and the radial wind speeds along the laser beam, it was necessary to analyze data acquired at higher frequencies than the time series of the 10-min mean values. Due to the fact that the lidar was streaming data at 50 Hz and the sonic was acquiring measurements at 32 Hz, two data sets were block averaged to create 10 Hz time series of wind speed values. Furthermore the data were separated in partitions of 1-hour length. The length of this time interval was chosen so as to ensure that it is long enough in order to contain all the turbulent fluctuations, but at the same time shorter than periods associated with diurnal effects. In the following table the wind characteristics (mean and standard deviation of the wind speed, turbulence intensity and mean and standard deviation of the wind direction) of 4 of these 1-hour periods are presented. These periods appears to contain stationary data of the wind speed and additionally the wind direction is observed to be generally stable. Furthermore for these wind directions it can be assumed that the sonic anemometer is not affected from any met mast wakes (see Appendix A). Histograms and time series of the speed and direction of the wind for each one of these cases are presented in the Appendix B.

Time interval [HH:MM]	$\bar{v}_r[\mathrm{ms}^{-1}]$	$\sigma_{v_r}[\mathrm{ms}^{-1}]$	$\sigma_{v_r}/\bar{v}_r[\%]$	Dir$[^o]$	$\sigma_{\mathrm{Dir}}[^o]$
12:20 - 13:20	11.1	1.3	11.6	290.5	5.2
13:30 - 14:30	11.5	1.1	9.1	292.2	5.4
16:40 - 17:40	9.3	0.9	10.5	284.2	5.9
18:40 - 19:40	7.8	1.2	15.5	267.6	6.4

Table 4: Wind characteristics of four periods, each one with a duration 1 hour.

Figure 14 presents the correlation diagram of the wind speed as measured by the sonic anemometer and the lidar during the period 16:40 - 17:40 on the 2009-05-05. The mean wind direction was found to be equal to 284.2°, which is approximately the same as the direction of the line-of-sight of the lidar. In the correlation diagram it is observed that the lidar is measuring slightly higher wind speeds than the sonic at wind speeds (6 - 8 ms^{-1}) and on the contrary slightly lower at higher wind speeds (9 - 13 ms^{-1}). A linear fit ($y = \alpha x + \beta$) was applied in this data set and was found that the data points were following the equation $y = 0.877x + 1.036$ (red line in Figure 14), indicating that the lidar is measuring slightly lower wind speeds than the sonic anemometer. In Figure 15 a part containing 2000 measurements is presented, where it can be seen that the lidar (purple line) is unable to follow some of the fluctuations of the wind speed as recorded by the sonic anemometer (blue line). In particular this is observed in cases were high frequency gusts (rapid changes of the wind speed) are occurring. The correlation diagrams from each of the periods presented in Table 4 can be found in Appendix C.

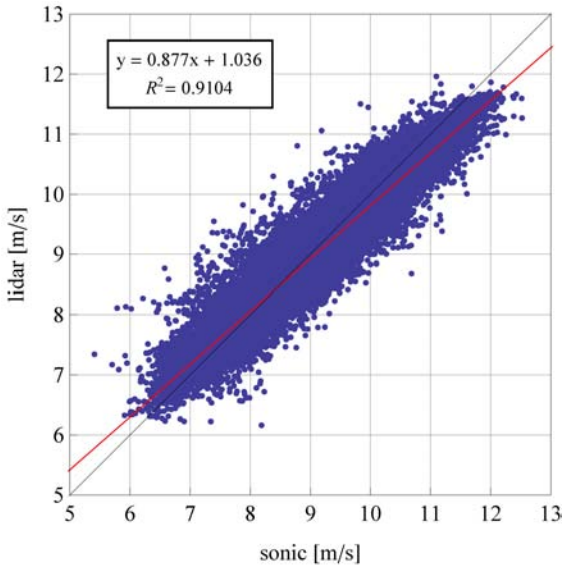

Figure 14: Correlation diagram between the 10 Hz time series of the wind speed measured by the lidar and by the sonic anemometer (red line: linear fit, black line: an line which indicates the y = x function).

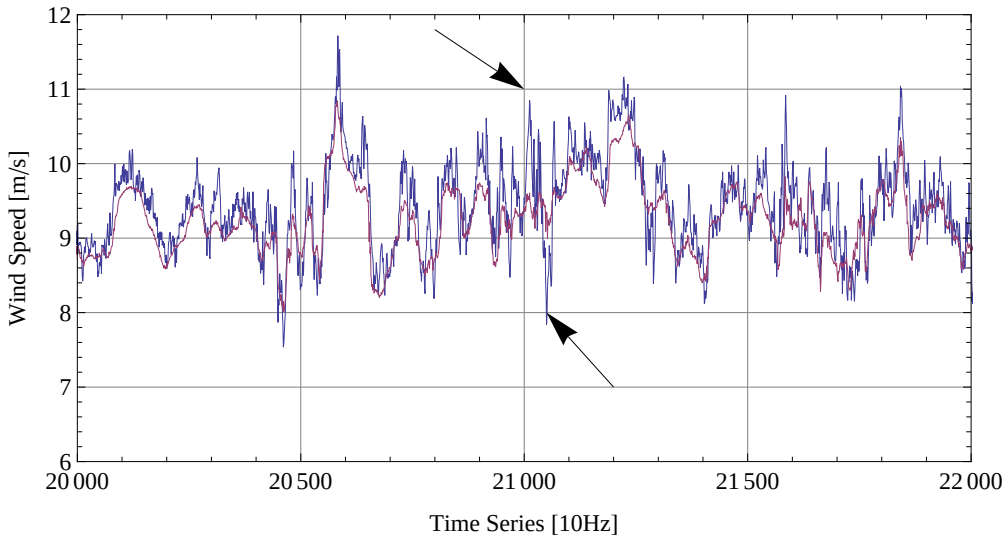

Figure 15: A part of the time series (10 Hz) of the wind speed measured from the lidar (purple line) and the sonic anemometer (blue line), during the period 16:40 - 17:40 on the 2009-05-05.

3.3 Spectral analysis

The turbulent fluctuations of the wind speed are characterized by various frequencies and wavelengths, which define the variance of the wind speed and can be determined by means of spectral analysis. In particular, the amplitude of the turbulent fluctuations at different frequencies can be studied through the power spectral density. The power spectral density (S) can be derived from the Fourier transformation of the covariance (R_u) between two point measurements separated by a distance x_1:

$$S_v(f) = \int_{-\infty}^{+\infty} R_v(x_1)\, e^{-2\pi i x_1 f} dx_1 \tag{8}$$

Figure 16 presents the frequency dependent power spectral density of the wind speed time series, for each of the periods given in Table 4. The spectra are logarithmically smoothed and the frequency band spans from 1.67 mHz until 5 Hz, corresponding to fluctuations with periods between 10 minutes and 200 ms. The analysis was performed using the 10 Hz mean values of the wind speed, for both the measurements of the lidar $S_{v_r}(f)$ and of the sonic anemometer $S_{v_s}(f)$. In order to reduce the uncertainties in the power spectral density the investigated 1-hour time periods were divided into 10-min intervals and the spectral results of each of them were subsequently averaged.

It is evident that the highest contribution to the variance of the wind is found in the lower frequency range (cycles with approximately 10-min periods). The lidar spectra $S_{v_r}(f)$ are in all the cases following the sonic spectra $S_{v_s}(f)$ up to frequencies of approximately 0.03 Hz. Above that frequency the lidar spectrum decreases more abruptly than the sonic spectrum, until it reaches frequencies of almost 2 Hz. This trend can be attributed to the spatial weighting effect that characterizes the lidar measurements. However, above 2 Hz an increase of the amplitude of the lidar spectra is observed, probably due to noise introduced to the lidar Doppler spectra.

Additionally the spectra of the wind speed measured by the sonic anemometer features a spike in the frequency band between 3 and 4 Hz, which could correspond to the vibrations of the met mast, which is subject to react to changes of the direction and the speed of the wind.

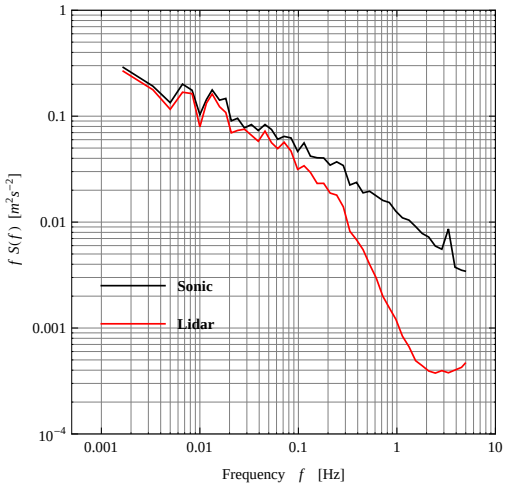

(a) 12:20 - 13:20

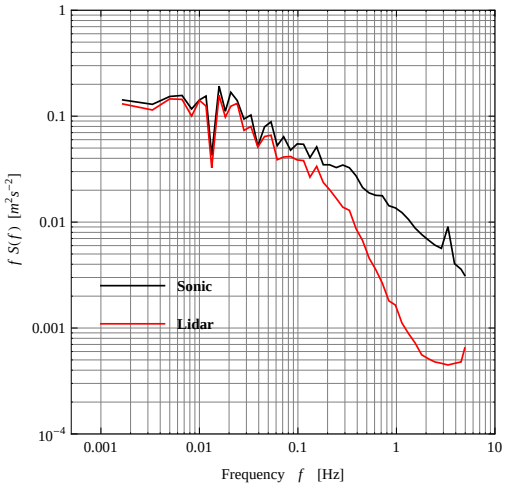

(b) 13:30 - 14:30

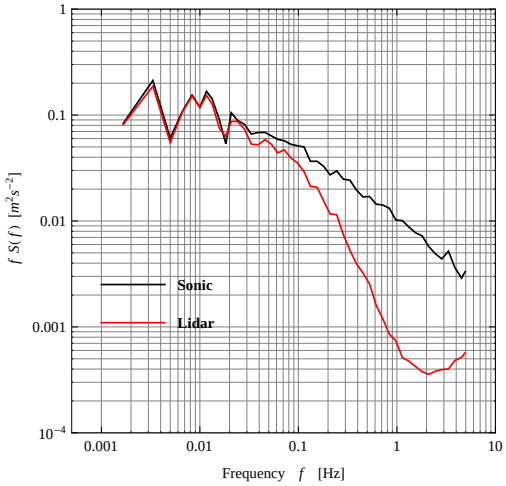

(c) 16:40 - 17:40

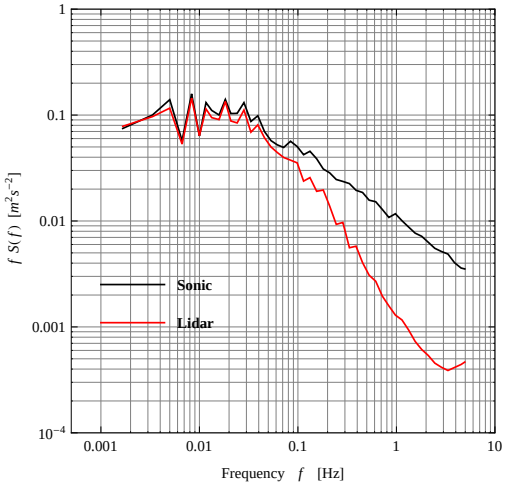

(d) 18:40 - 19:40

Figure 16: Spectra of the time series of the wind speed as measured by the lidar (red) and by the sonic anemometer (black) on the 2009-05-05.

3.3.1 Spectral transfer function

The filtering due to the spatial averaging effect of the lidar measurements is considered to have the same effect as a low-pass filter, which passes low frequencies signals and attenuates all signals, above a certain frequency. This means that a frequency limit is expected in the detection of the turbulent fluctuations of the wind speed by the lidar. In this section the spectral transfer function, which represents the turbulence attenuation, that is observed in the lidar measured Doppler spectra, is calculated through both (a) the power spectral density and (b) the cross-spectrum of the sonic anemometer and lidar wind speed measurements.

3.3.2 Spectral ratio

The first approach for the calculation of the spectral transfer function is based on the assumption that the spatial weighting average effect of the lidar measurements is occurring over exactly the same turbulent fluctuations as those detected by the sonic anemometer. Subsequently using the equation (8) it can be shown that the ratio between the wind speed spectra measured by the lidar and by the sonic anemometer is equal to the absolute square of the Fourier transform of the spatial weighting function $|\hat{\varphi}(k)|^2$ (for a detailed description see Appendix D). The Fourier transform of the spatial weighting function (see equation 6) is equal to an exponential function which depends on the wavenumber (k) and the Rayleigh length (z_R) according to:

$$\frac{S_{v_r}(k)}{S_{v_s}(k)} = |\hat{\varphi}(k)|^2 = e^{-2|k|z_R} \tag{9}$$

Figure 17 presents the spectral transfer function for each of the time periods specified in Table 3. The spectral transfer function is presented as a function of the wavenumber k (m^{-1}), which is a measure of the size of the turbulence eddies. It can be observed that for wavenumbers below approximately 0.01 m^{-1}, the lidar is following the turbulence fluctuations measured from the sonic relatively well, with spectral transfer function values between 0.9 - 1.0. However the general tendency is that the spectral transfer function is smaller than 1.0, which could be explained by fluctuations of the wind direction, which alter the projection of the wind vector to the line-of-sight of the lidar (lidar's line-of-sight direction: 283°). Moreover it is observed that the larger the drift of the wind direction from the line-of-sight of the lidar is, the smoother is the decrease of the spectral transfer function.

Additionally, an attempt to model the spectral transfer function was performed. Two different formulas have been tested for the Rayleigh length (z_R) in equation (9), in accordance with Figure 3. The theoretical spectral transfer functions (each one for different Rayleigh length values) are depicted with a black solid and dashed line, for z_R equal to $0.00085 \cdot r^2$ and $0.0013 \cdot r^2$, respectively. It is observed that the measured spectral transfer functions are presenting a deviation from both the two theoretical curves, which could be an indication of a different beam divergence from the optical fiber end than the expected one.

3.3.3 Cross-spectrum

An additional approach to the calculation of the spectral transfer function $\hat{\varphi}(k)$ is through the cross-spectrum ($X_{v_r v_s}$) of the lidar and the sonic anemometer measurements. The cross-spectrum of two signals is defined as the convolution of the Fourier transform of one of the signals with the conjugated Fourier transform of the other signal:

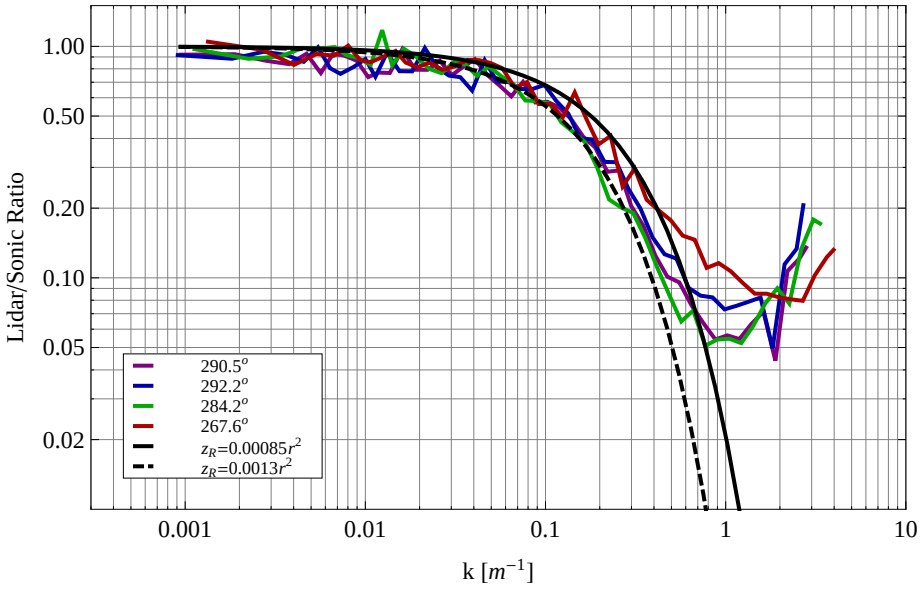

Figure 17: Ratio between the spectra of the turbulence fluctuations of the wind speed, measured by the lidar and the sonic anemometer (values logarithmically smoothed).

$$\begin{aligned} X_{v_r v_s}(k) &= \langle \hat{v}_r(k) \hat{v}_s^*(k) \rangle \overset{(5)}{=} \langle \hat{\varphi}(k)\, \hat{v}_s(k)\, \hat{v}_s^*(k) \rangle \\ \Rightarrow X_{v_r v_s}(k) &= \hat{\varphi}(k)\, S_{v_s}(k) \end{aligned} \tag{10}$$

When separating the equation (10) into the real and the imaginary part, it is found that:

$$Re(X_{v_r v_s}(k)) = \hat{\varphi}(k) \cdot S_{v_s}(k)$$

and

$$\frac{Im(X_{v_r v_s}(k))}{S_{v_s}(k)} \approx 0 \tag{11}$$

Therefore the weighting spatial function can be calculated through the ratio:

$$\hat{\varphi}(k) \approx \frac{Re(X_{v_r v_s}(k))}{S_{v_s}(k)} \tag{12}$$

Figure 18 presents the spectral transfer function values as calculated using the equation (12). It is generally observed less scattering than the first approach, with values between 0.9 and 1.0 for wavenumbers below 0.03 m^{-1}. Above that point the spectral transfer function degrades, following an exponential function of the Fourier transform of the spatial weighting function. It is observed that the theoretical spectral transfer function with a Rayleigh length of $z_R(r) = 0.0013\, r^2$ better describes the evolution of the spectral transfer function, which corresponds to an effective beam radius of the telescope of the ZephIR prototype of 19.5 mm.

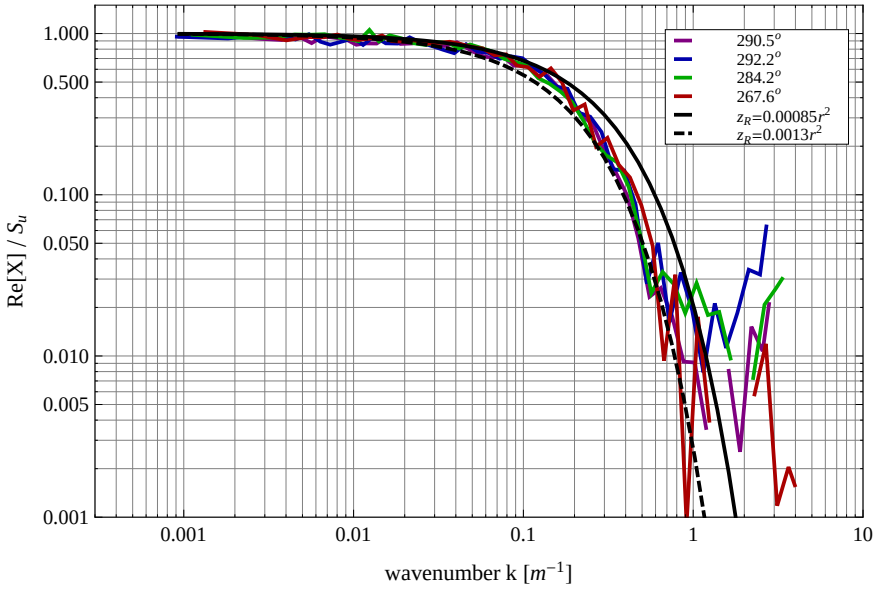

Figure 18: Ratio between the real part of the cross spectrum of the sonic and lidar wind speed time series and sonic spectrum (values logarithmically smoothed).

Moreover, it is observed that between wavenumbers 0.03 and 0.3 m^{-1} the measured spectral transfer function is deviating from the two theoretical ones (see Figure 19). This can be occurring because either the spatial weighting function cannot be exactly represented by a Lorentzian function [14] or because the beam divergence from the optical fiber end to the telescope of the lidar is slightly different from the ones proposed.

A cross-correlation between the spectral transfer function measured for a wind direction of 282.4° (green solid line in Figures 18), which is the closest to the line-of-sight of the lidar (283°), and the spatial weighting function (equation (9)) has indicated that the best correlation could be achieved for a Rayleigh length formula equal to $z_R(r) = 0.0015\ r^2$, which corresponds to an effective radius of the telescope of 18.5 mm. It is noted that the calculation of this value is dependent on the accuracy of the USA-1 sonic anemometers flow distortion correction method.

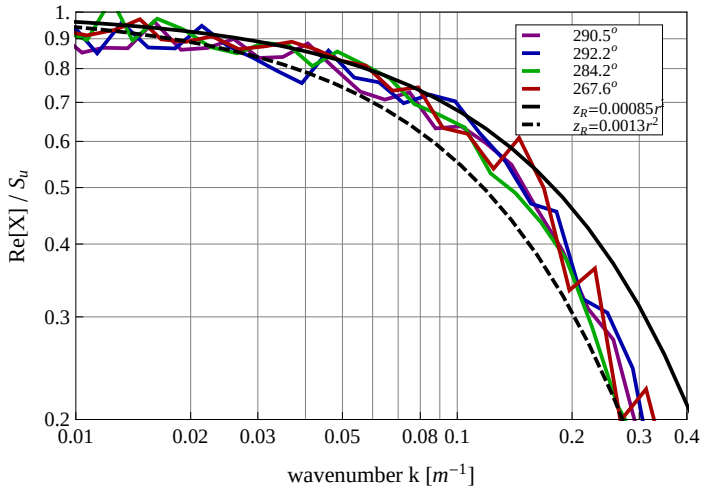

Figure 19: Zoomed area of the Figure 18 between the wavenumbers 0.01 and 0.4 m^{-1}.

Figure 20 presents the ratio of the equation (11) as function of the wavenumber. As expected the values are close to 0 for all the wavenumbers.

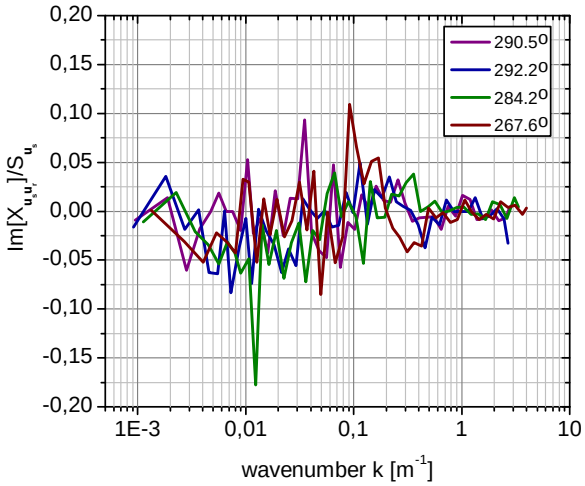

Figure 20: The imaginary part of the cross spectrum of the sonic and the lidar wind speed time series divided by the sonic spectrum.

Moreover through the cross spectrum it is possible to verify if a phase shift is present between the sonic anemometer measurement and the lidar measurements, which could introduce a bias in the spectral analysis. Doing so, the phase spectrum was calculated through the argument of the cross-spectrum:

$$\arg\varphi = \frac{Re(X_{v_r v_s}(k))}{Im(X_{v_r v_s}(k))}$$

The phase spectrum is presented in Figure 21, where it can be observed that there are no time delays between the data. The phase spectrum has a phase of about 0 for wavenumbers below 0.4 m^{-1}, above which a scattering is observed due to noise, attributed to the incoherence of the small turbulent structures detected by the lidar and the sonic anemometer.

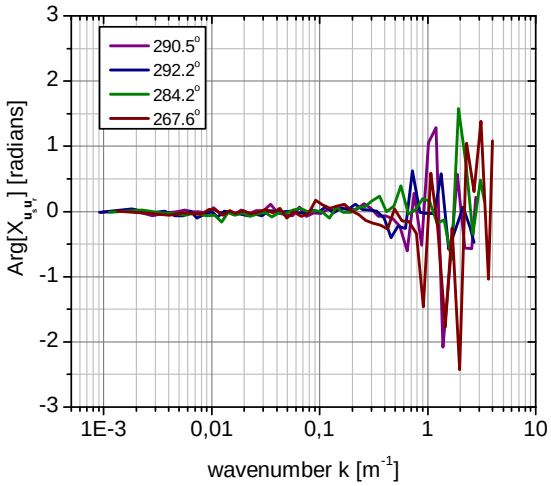

Figure 21: Phase spectrum.

3.4 Deconvolution

The lidar wind speed measurements are affected by the spatial averaging effect, which occurs over the probe volume. Thus, the lidar measured wind speed can be considered as the convolution of the wind speed with the spatial weighting function, as presented in equation (5):

$$v(x) = \int_{-\infty}^{\infty} \varphi(s)\mathbf{n} \cdot u(s\mathbf{n} + x)ds$$

Due to this effect a lower spatial resolution is anticipated when comparing the measurements of the lidar with the ones of the sonic anemometer. This was verified after performing a spectral analysis as presented in Section 3.3. The effect of the spatial weighting function can in theory be removed by a deconvolution of the lidar signal. The deconvolution of a signal from a filter function can in principle be achieved by dividing the Fourier transform of the signal with the Fourier transform of the filter [16].

An attempt to achieve such a deconvolution is presented in this section. First a theoretical model is being proposed and tested using a simulated time series of the wind speed. Subsequently, an attempt is made to validate this model, using the data set acquired from the ZephIR lidar prototype, during the measurement campaign on the 2009-05-05.

3.4.1 Theory

The Doppler spectrum $S(v,t)$ is a function of time (t) and the wind speed component v along the beam $v = u \cdot \mathbf{n}$, and can be written as:

$$S(v,t) = \int_{-\infty}^{\infty} \varphi(s) \cdot \delta\left(v + \mathbf{n} \cdot u(s\mathbf{n}, t)\right) ds \tag{13}$$

Where δ is the Dirac delta function. The investigation is narrowed to the case where the lidar is pointing directly upwind, i.e. $n = (-1, 0, 0)$. Furthermore the Taylor's "frozen turbulence" hypothesis is assumed to be valid giving the simplification:

$$u(x, y, z, t = 0) = u(x + Ut, y, z, t) \tag{14}$$

The wind field at any given time can be obtained by translating the wind field at $t = 0$. In this case equation (13) can be reduced to:

$$S(v,t) = \int_{-\infty}^{\infty} \varphi(s) \cdot \delta\left(v + \mathbf{n} \cdot u_1(s, 0, 0, t)\right) ds \tag{15}$$

The notation is easier if the spectrum S is written not as a function of time t but rather of space x by invoking Taylor's hypothesis, which gives

$$S(v,x) = \int_{-\infty}^{\infty} \varphi(s) \cdot \delta\left(v - u(s - x)\right) ds \tag{16}$$

with $u(s - x) = u_1(s, 0, 0, t = x/U)$. It can be noticed that equation (16) is a convolution of the weighting function $\varphi(s)$ and the delta function $\delta(v - u(s - x))$. Therefore, in principle, it is possible to deconvolute both sides of (16) to obtain $\delta(v - u(x))$ and from that $u(x)$ with no spatial filtering.

In practice, the deconvolution can be achieved through the deconvolution of the time series of signal intensity per bin (f_{bin}). Each Doppler spectrum is depicted in a bandwidth of 25 MHz, separated in 256 bins.

The deconvolution can be achieved through the calculation of the ratio between the Fourier transforms of the spectral intensity per bin (f_{bin}) and the spatial weighting function (φ):

$$\hat{f}_{bin_{deconv}}(f) = \frac{\hat{f}_{bin}(f)}{\hat{\varphi}(f)}, \quad \text{where } bin = 1, 2, ..., 256. \tag{17}$$

Consequently, the inverse Fourier transform of the equation (17) will give the deconvoluted signal. Possible implications are arising through this approach due to noise effects. In general when noise is added to the signal after a low pass operator, it will be amplified when the Fourier transform of the signal is divided by the Fourier transform of the low pass operator. The high frequency components of the low pass filter are small, which leads to high amplitudes at high frequencies in the resulting deconvoluted signal.

Prior to the calculation of the inverse discrete Fourier transform (DFT), the convoluted signal has to be thresholded. This is necessary due to the fact that the DFT of the spatial weighting function contains a lot of values which are close to zero. In order to avoid the high values which would result from it's inversion a threshold is applied.

In the above equation a window is applied in order to deconvolve only a certain bandwidth (frequency band). This is defined by the f_ω. The window function $W(f)$ is selected to be a Gaussian function (see Figure 22):

$$W(f) = \begin{cases} e^{-\frac{1}{2}\cdot\left(\frac{f}{f_\omega}\right)^2}, & \text{if } \frac{f}{f_\omega} \leq 10 \\ \\ 0, & \text{if } \frac{f}{f_\omega} > 10 \end{cases} \tag{18}$$

Where f_ω is defined as the inverse filter length of the Guassian filter. The higher this inverse filter length is the closer $W(f)$ to a full inverse filter.

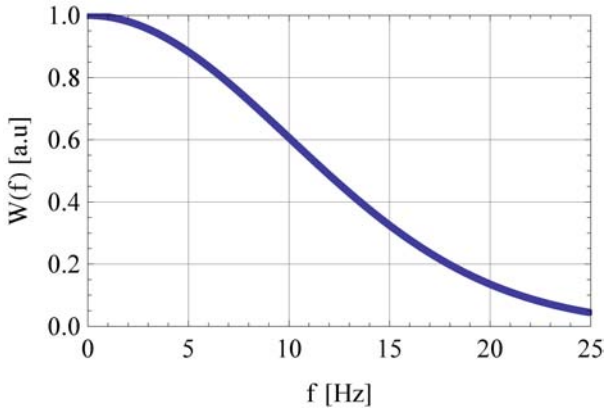

Figure 22: Gaussian function used for thresholding the deconvolution.

$$\hat{f}_{bin_{deconv}}(f) = \frac{\hat{f}_{bin}(f)}{\hat{\varphi}(f)} \cdot W(f) \tag{19}$$

In practice, noise is preventing the complete removal of the filtering effect and the purpose of this study is to investigate how much of the filtering can be removed.

3.4.2 Simulation

The first assumption in order to make a simulation is, that the turbulent fluctuations in the direction of the mean wind can be described by the Kaimal spectrum [17].

$$S_u(f) = u_*^2 \frac{52.5z/U}{(1+33fz/U)^{5/3}} \tag{20}$$

Where U is the mean wind speed, z is the height above ground, f is the frequency, and u_* is the friction velocity. Since this spectrum is double-sided, the integral from $-\infty$ to ∞ of $S_u(f)$ corresponds to the variance of the wind speed time series. Based on this spectrum, a Gaussian time series of the wind fluctuations was simulated [18]. For the simulation it was chosen $U = 10$ m/s, $u_* = 0.5$ m/s, $z = 30$ m, and the time resolution was $\Delta t = 0.01$ s (sampling rate: 100 Hz) corresponding to a spatial resolution of $\Delta x = U\Delta t = 0.1$ m. A 10-minutes period of data corresponding to a simulation length of 6 km were simulated. Consequently using equation (16) the corresponding lidar Doppler spectra of the 100 Hz wind speed values were created. A small fraction of those are presented to the left in figure 23. To the right in the same figure is the corresponding Doppler spectrum calculated from the curves in the left plot using the equation (16). For the calculation of the Doppler spectra, a Lorentzian spatial weighting function has been used. The spatial averaging was assumed to extend 30 m away from the focal point in both directions (towards and away from the lidar).

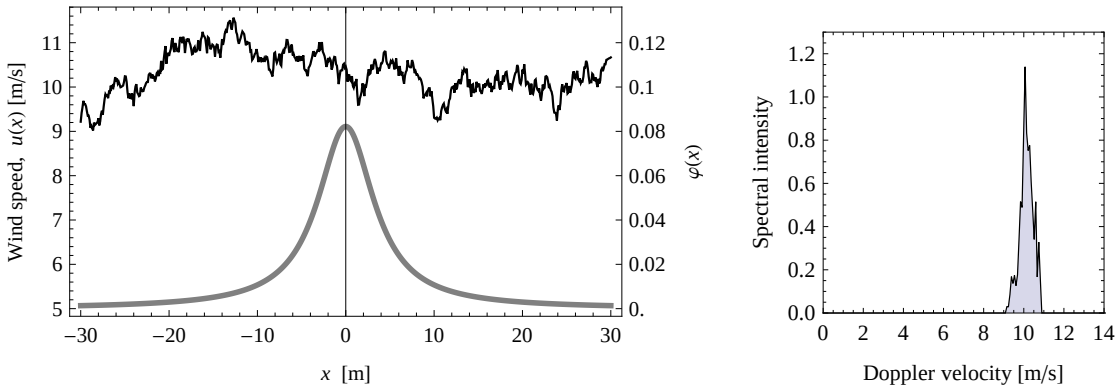

Figure 23: Left: A part of the simulated wind time series (black) and the spatial sensitivity function $\varphi(x)$ from (6) with $z_R = 3.9$ m (focus distance: 67.5 m). Right: The corresponding Doppler spectrum calculated according to equation (16).

Thirty seconds of the ten minute simulated Doppler spectra are shown in figure 24 (top). The figure presents the spectral density per bin. The darker the shades are indicated the higher is the spectral density. In figure 24 (bottom) the corresponding deconvoluted bin signals are presented. It can be seen that for this period the corresponding bin number to the wind fluctuations are varying between 100 and 160. Through the comparison of the two plots it can be observed that the deconvoluted time series are indicating a higher spectral density. Moreover it is observed a "scattering" in the first and the last parts of the time series, which is produced during the step of the calculation of the inverse Fourier transform.

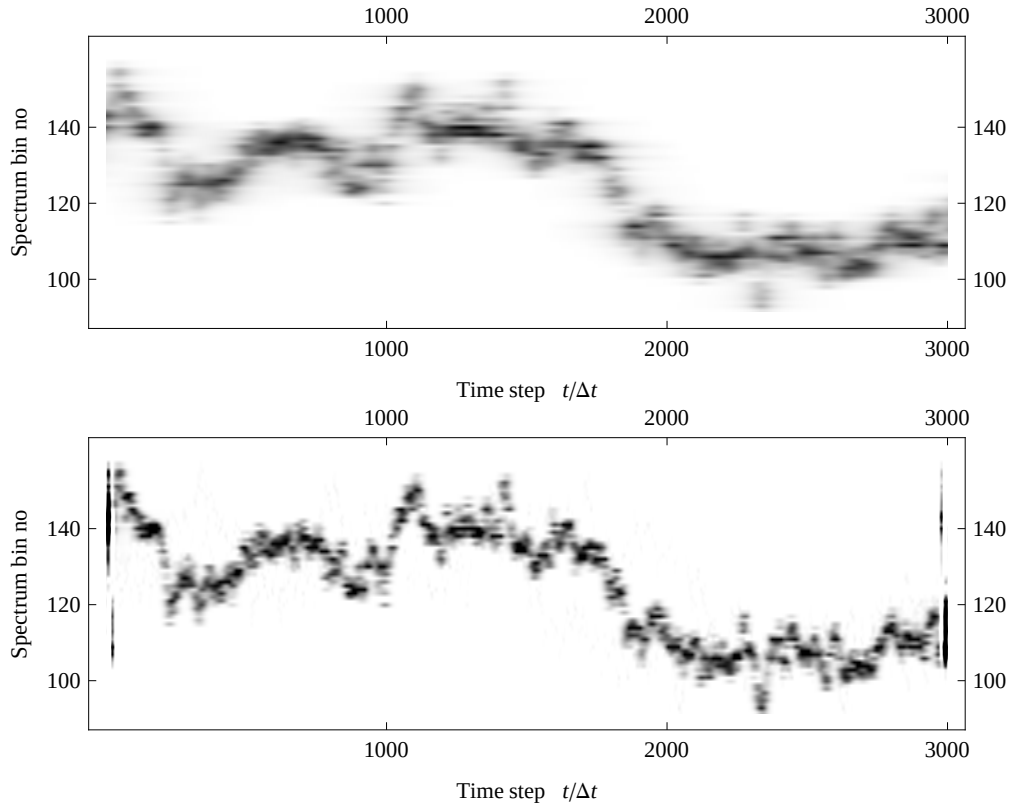

Figure 24: Simulated Doppler spectra for 30 seconds ($\Delta t = 0.01$ s). Top: The original simulated data based on the equation (16). Bottom: Deconvoluted data according to equation (19)

The corresponding wind speed to the convoluted and deconvoluted spectra were calculated, by the means of 3 different Doppler frequency estimators (*max*, *centroid* and *median*). The *max* estimator finds the frequency bin containing the maximum intensity of the signal, whilst the *centroid* and *median* frequency estimators use a centroid and median function, respectively for the derivation of the Doppler shift bin. Figure 25 presents 30 sec of these time series, where it is observed that the lidar wind speed time series calculated from the convoluted spectra does not manage to follow all the fluctuations of the simulated unfiltered time series. Two such cases are indicated with arrows in the upper plot. However when the frequency estimators are applied to the deconvoluted spectra these deviations do not appear. Additionally it is observed that the scattering in the spectral density which appeared in the figure 23, is transfered to the calculation of the wind speed time series, where the deconvolution is creating an extreme variation in the outcome of the frequency estimators result, i.e. 0 - 1 sec and 29 - 30 sec in figure 25 (bottom).

The improvement of the lidar's resolution can also be observed in the calculation of the standard deviation (σ_{u-v}) of the absolute difference between the simulated wind speeds (u) and the wind speeds extracted from the Doppler spectra (v).

$$\sigma_{u-v} = \sqrt{\frac{\sum_{i=1}^{n} \left((u_i - v_i) - \mu_{u-v}\right)^2}{n-1}} \tag{21}$$

Table 5 presents the values of this standard deviation (σ_{u-v}), where a decrease in the standard deviation can be seen. The lower values of the standard deviation are appearing in the *median* frequency estimator.

	Maximum	Centroid	Median
Standard	0.28	0.3	0.27
Deconvoluted	0.2	0.21	0.18

Table 5: The root mean square difference between the 100 Hz simulated wind signal and the wind derived from the simulated Doppler spectra.

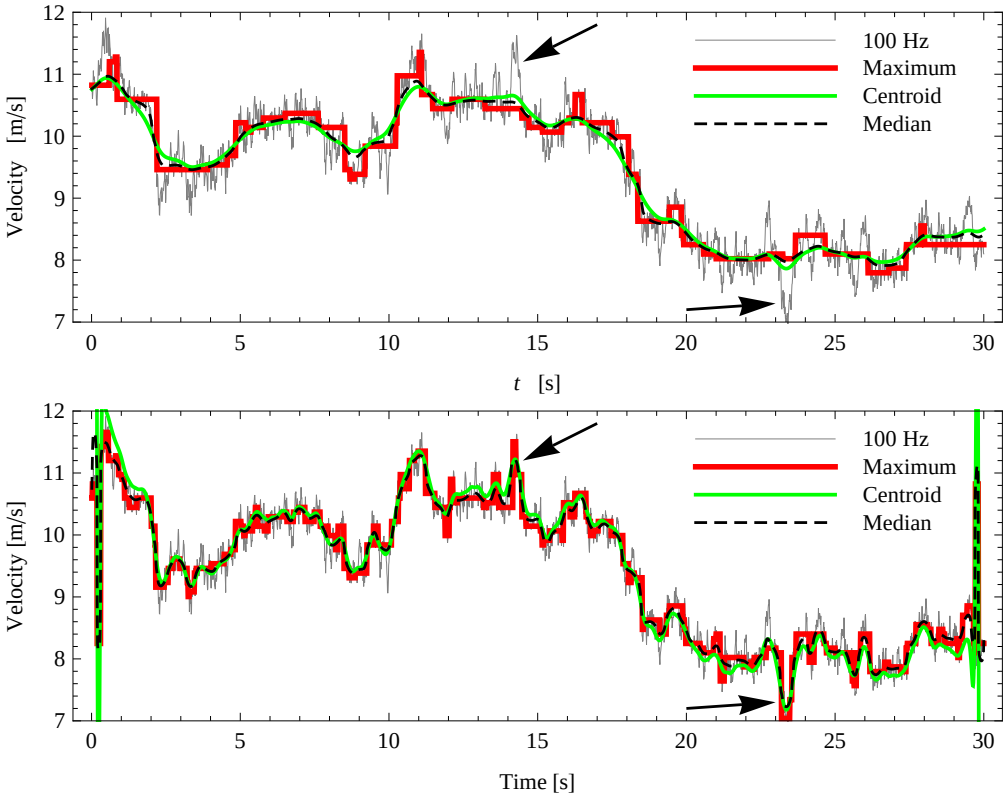

Figure 25: The 100-Hz wind speed for the same period as in figure 24 in a thin, gray line. Top: Wind speed from the Doppler spectra. Bottom: Wind speeds from the deconvoluted Doppler spectra.

Figure 26 presents the power density spectra of the analyzed velocities for both the convoluted (left) and the deconvoluted (right) Doppler spectra. It can be observed that the spectra of the lidar wind speed are following the simulated time series until the frequencies of about 0.1 Hz. However the deconvoluted one is increasing the resolution until almost 1 Hz. This can be considered as an indication that it is possible to detect faster wind speed fluctuations, if the lidar signal is deconvoluted.

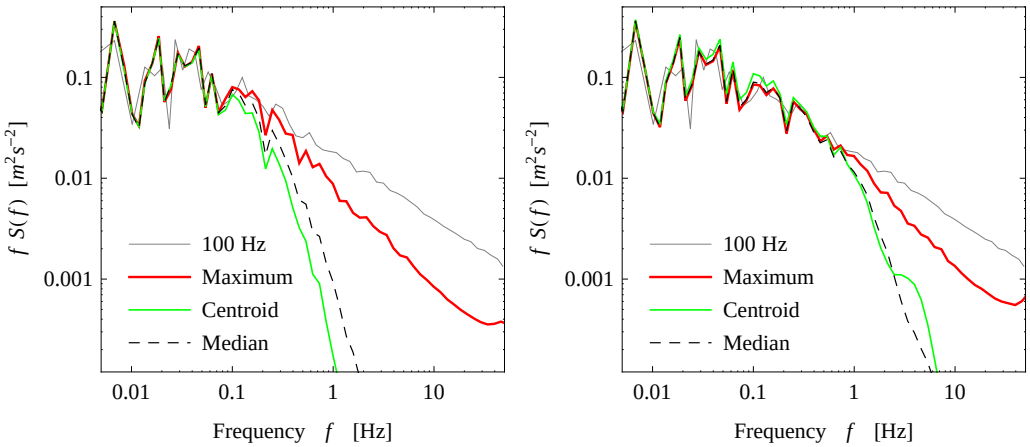

Figure 26: Spectra of the 10 minutes velocity time series. Left: Analyzed from the original Doppler spectra. Right: Analyzed from the deconvoluted Doppler spectra.

3.4.3 Model validation

For the validation of the deconvolution method a time series of real lidar wind speed measurements were used. Specifically, the period between 17:30 and 17:40 on the 2009-05-05 was selected, where the wind was blowing along the line-of-sight of the lidar ($\mu_{Dir} = 282.16°$ and $\sigma_{\mathrm{Dir}} = 3.70°$).

In Figure 27 the time series of the wind speed as measured by the sonic and the lidar are presented. The wind speed was calculated from the Doppler spectra measured by the lidar, using the three different frequency estimators presented in section 3.4.2. It is observed that even after the deconvolution of the lidar signal, no improvement in the accuracy of the lidar measurements is achieved. This is also depicted in table 6 where the corresponding standard deviations are presented.

	Maximum	Centroid	Median
Standard	0.32	0.31	0.31
Deconvoluted	0.33	0.32	0.31

Table 6: The root mean square difference between the 10 Hz sonic wind speed measurements and the wind derived from the lidar's Doppler spectra.

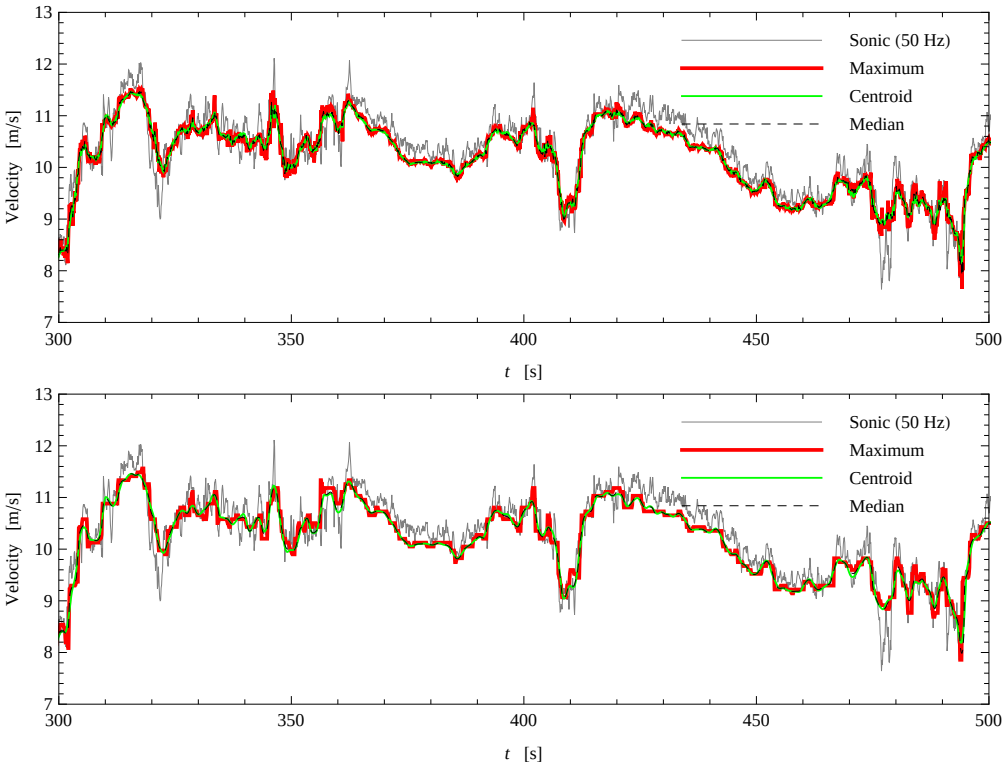

Figure 27: The 10-Hz wind speed time series as measured by the sonic anemometer (gray) and by the lidar (red, green, black) using 3 different frequency estimators for the Doppler shift. Top: Wind speed from the Doppler spectra. Bottom: Wind speeds from the deconvoluted Doppler spectra.

Additionally when comparing the frequency spectra (see Figure 28) it is observed that there is not a significant change in the distribution of the power spectral density. The reduction of the noise contribution to the power spectral density which is observed in the deconvoluted spectra (right) is an effect of the window function W(f) (see equation (18)).

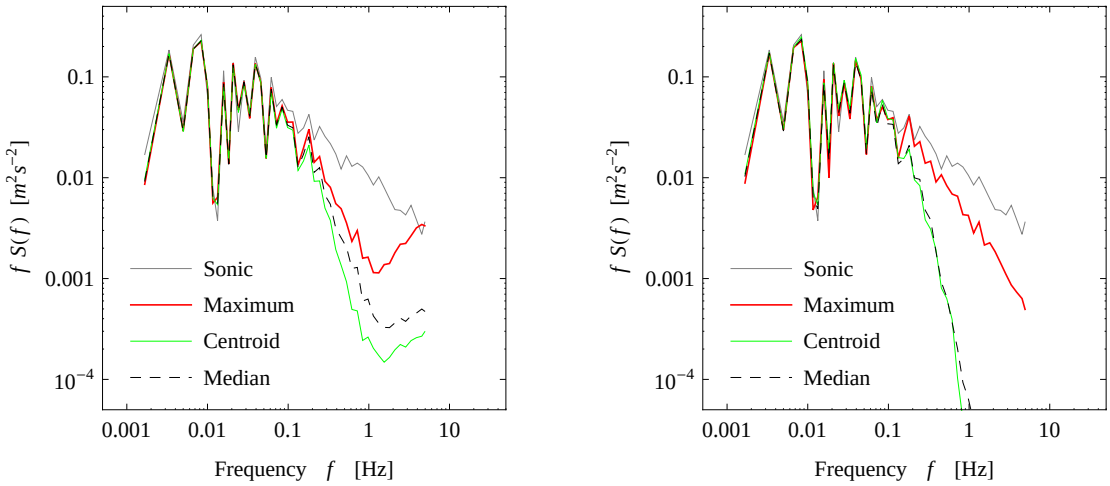

Figure 28: Spectra of the 10-minutes measured velocity time series. Left: Analyzed from the original Doppler spectra. Right: Analyzed from the deconvoluted Doppler spectra.

4 Conclusion

In this report the spectral characteristics of the wind speed as measured by two different instruments, a ZephIR prototype lidar and a METEK sonic anemometer were investigated. The ZephIR prototype lidar was mounted on the nacelle of a Vestas V27 wind turbine, while the METEK sonic anemometer was installed on a nearby located meteorological mast. The data analysis was focused on time intervals where the wind flow coincided with the line-of-sight of the lidar, thus minimizing the effect of the wind direction fluctuations to the detection of the wind speed turbulence.

The lidar was operating in a staring mode and the focus distance was set to 67.5 m, which corresponded to the distance between the wind turbine and the met mast. The focal point of the lidar was expected to be approximately 1 m above the position of the sonic anemometer, hence it can be assumed that the two instruments were measuring in almost the same location. Therefore it was possible to compare the spectral characteristics of two different measurement concepts, a point (sonic anemometer) and a volume averaging (lidar) measurement using data with the same temporal resolution (10 Hz).

The regression analysis between the lidar and the sonic anemometer was performed using both 10-minutes and 10-Hz wind speed values. A high correlation was observed on the 10-minutes mean values with a R^2 value of 0.9996. This correlation was not degraded even if mean wind values as low as 2 ms^{-1} were included in the analysis. In the 10-Hz regression analysis a larger dispersion of the data was observed, thus decreasing the correlation $R^2 \sim 0.91$ - 0.94, this tendency is explained by the averaging volume of the lidar.

Regarding the spectral analysis the lidar wind speed measurements displayed a lower temporal resolution than those measured by the sonic anemometer. It was observed that the lidar was adequately measuring the turbulence fluctuations with wavenumbers below 0.01 - 0.03 m^{-1}. This limitation is attributed to the fact that the lidar measurements result from a convolution of the wind speed with a spatial weighting function, which acts in a similar fashion to a low pass filter. The study of the spectral transfer function of the lidar measurements indicated that the effective radius of this specific prototype ZephIR's telescope could be considered to be between 18.5 and 19.5 mm. These results are subject to the accuracy of the USA-1 sonic anemometer flow distortion correction.

Additionally an attempt to reverse (deconvolve) the effect of the low pass filter was performed, using the Fourier transform of the spatial weighting function. When applied to simulated time series the deconvolution improved the spectral resolution of the lidar measurements and the standard deviation of the difference between the lidar and sonic anemometers wind speed measurements was decreased. However when the real wind speed data were deconvoluted the reduction of the corresponding standard deviation was insignificant.

5 Discussion

The wind lidars are considered as potential candidates for the active control of a wind turbine, therefore it is necessary to investigate which parameters and at what magnitude are effecting the precision and the accuracy of these systems.

From the spectral analysis the ZephIR prototype lidar it was observed a limited capability in the detection of the turbulent structures of the wind speed, thus decreasing the precision of the system in detecting fast fluctuations of the wind speed. However this is not expected to affect applications, where average values of the wind speed over a long time period (i.e 10 minutes) are used, such as the study of power performance of the wind turbine (power curve analysis).

The spectral transfer function which describes the turbulence attenuation of the wind speed induced in the lidar measurements, can be used for the determination of the applications in which a lidar could be utilized for optimizing the wind turbine control. The results of the spectral transfer function presented in this report, are expected to be trustworthy only if the hypothesis, that both the lidar and the sonic anemometer were measuring in the same air volume and thus probing simultaneously the same wind fluctuations, is valid. The deviations of the measured spectral transfer function from the theoretical model developed in this report are assumed that are caused from the stochastic variations of the wind direction, which are altering the projection of the wind vector to the the line-of-sight of the lidar. This parameter is expected to impose a limitation in the deconvolution of the lidar signals, and it is going to be a topic of further investigation.

6 Acknowledgement

The authors would like to gratefully acknowledge Per Hansen and Renè Kjærsgaard for their technical support. The experiment has been conducted as a part of the Work Package 6 of the Upwind project, which is part of the European Unions Sixth Framework Program (FP6).

References

[1] Emeis S., Harris M., and Banta R. M. Boundary-layer anemometry by optical remote sensing for wind energy applications. *Meteorologische Zeitschrift*, 16:337–347, 2007.

[2] Wagner R., Courtney M., Gottschall J., and Lindelöw. Improvement of power curve measurement with lidar wind speed profiles. In *EWEC 2010 Scientifc Proceedings*. EWEC, 2010.

[3] Harris M., Hand M., and Wright A. Lidar for turbine control. Technical Report, TP-500-39154, NREL, 2006.

[4] Harris M., Bryce D.J., Coffey A. S., Smith D. A., Birkemeyer J., and Knopf U. Advance measurement of gusts by laser anemometry. *Journal of Wind Engineering and Industrial Aerodynamics*, 95:1637 – 1647, 2007.

[5] Mikkelsen T., Hansen K. H., Angelou N., Sjöholm M., Harris M., Handley P., Scullion R., Ellis G., and Vives G. Lidar wind speed measurements from a rotating spinner. In *EWEC 2010 Scientifc Proceedings*. EWEC, 2010.

[6] Dakin E., Pal A., Belen F., and Küpper M. Boosting power production update. Technical report, Catch the Wind, 2010.

[7] Smith D. A., Harris M., Coffey S., Mikkelsen T., Jørgensen H. E., Mann J., and Danielian R. Wind lidar evaluation at the danish test site in Høvsøre. *Wind Energy*, 9:87–93, 2006.

[8] Courtney M., Wagner R., and Lindelöw P. Testing and comparison of lidars for profile and turbulence measurements in wind energy. In *IOP Conference Series: Earth and Enviromental Science 1*, 2008.

[9] Kapp S. Speed control of wind turbines by use of remote sensing technologies. Master's thesis, Engineering Cybernetics, University of Stuttgart, 2010.

[10] Mikkelsen T. On mean wind and turbulence profile measurements from ground-based wind lidars: limitations in time and space resolution with continuous wave and pulsed lidar systems. EWEC, 2009.

[11] Siegman A. E. *Lasers*. University Science Books, 1986.

[12] Wagner R., Mikkelsen T., and Courtney M. Investigation of turbulence measurements with a continuous wave conically scanning lidar. Research Report, Risø-R-1682(EN), Risø, 2009.

[13] Sjöholm M., Mikkelsen T., Mann J., Enevoldsen K., and Courtney M. Spatial averaging-effects on turbulence measured by a continuous-wave coherent lidar. *Meteorologische Zeitschrift*, 18:281–287, 2009.

[14] Sonnenschein C. M. and Horrigan F. A. Signal-to-noise relationships for coaxial systems that heterodyne backscatter from the atmosphere. *Applied Optics*, 10:1600–1604, 1971.

[15] Mann J., Cariou J. P., Courtney M., Parmentier R., Mikkelsen T., Wagner R., Lindelöw P., Sjöholm M., and Enevoldsen K. Comparison of 3d turbulence measurements using three staring wind lidars and a sonic anemometer. *Meteorologische Zeitschrift*, 18(2):135–140, 2009.

[16] Bendat J. S. and Piersol A. G. *Random data: Analysis and measurements procedures*. John Wiley & Sons, 4^{th} edition, 2010.

[17] Kaimal J., Wyngaard J., Izumi Y., and Cotè O. R. Spectral characteristics of surface-layer turbulence. *Quarterly Journal of the Royal Meteorological Society*, 98(417):563 – 589, 1972.

[18] Mann J. Wind field simulation. *Probabilistic Engineering Mechanics*, 13(4):269–282, 1998.

A Sonic - Cup anemometers comparison

A METEK sonic anemometer at the meteorological mast, was measuring the wind speed and direction throughout the whole duration of the experiment. The sonic anemometer was installed at a height of 32 m, mounted on a horizontal boom with a length of 2.5 m. In order to investigate the reliability of the instrument's performance, the measurements of the sonic were compared with those of a cup anemometer which was also found at the height of 32 m. Figure 29 presents the ratio of the sonic to cup wind speed measurements versus the direction of the wind, measured by the sonic anemometer. For the calculation of this ratio there were used data acquired during the period 2009-04-01 - 2010-03-01. The data were filtered in order to take into account only wind speed measurements above 4 ms^{-1}. Moreover a limit of acceptance was applied in the filter, regarding the atmospheric temperature. A minimum temperature of 2°C was selected, in order to mitigate the possibility of taking into account cup anemometer data from periods where the cup was frozen.

In the figure reffig:soniccupcomp the shadow effect of the met mast on the sonic and the cup measurements can be observed for different wind directions. Between 5°and30° the cup is underestimating the wind speed, while the contrary is happening between the directions 175°and200°. Furthermore for directions between $70° - 130°$ the met mast is found in the wake of the adjacent V27 wind turbine.

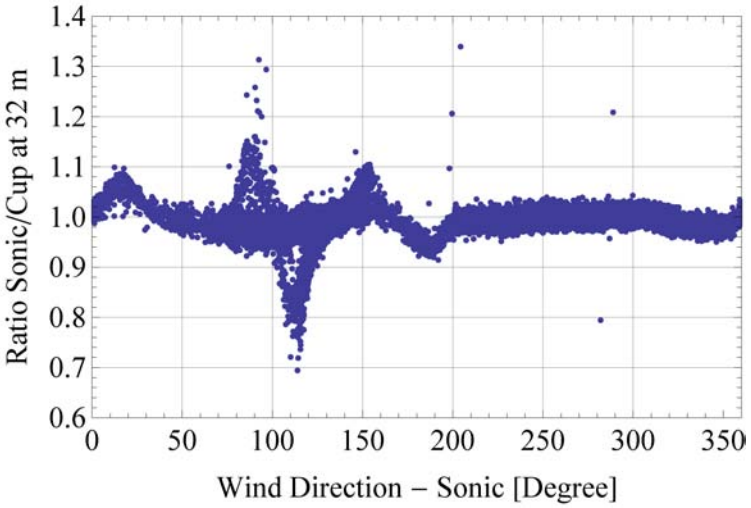

Figure 29: Sonic to Cup anemometer ratio of the wind speed measurements at 32 m.

B Wind speed and direction time series

B.1 Period A (2009-05-05 12:20 - 13:20)

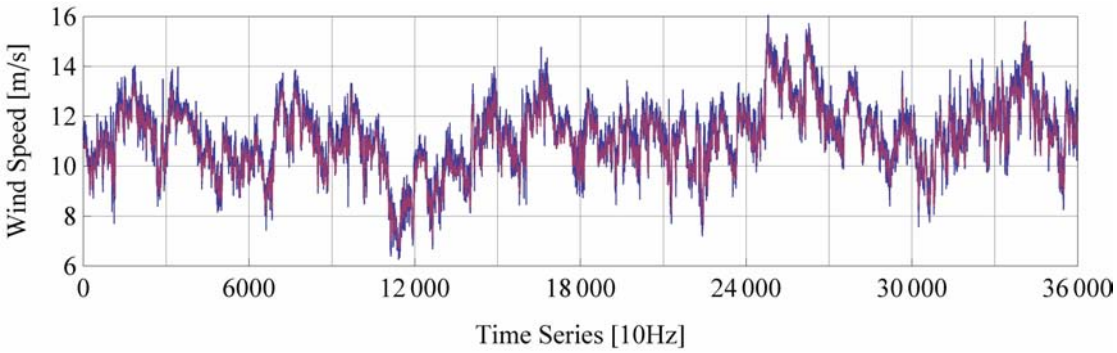

Figure 30: Time series (10 Hz) of the wind speed as measured by the ZephIR lidar (purple line) and by the Metek sonic anemometer (blue line), during the period 12:20 - 13:20, on the 2009-05-05.

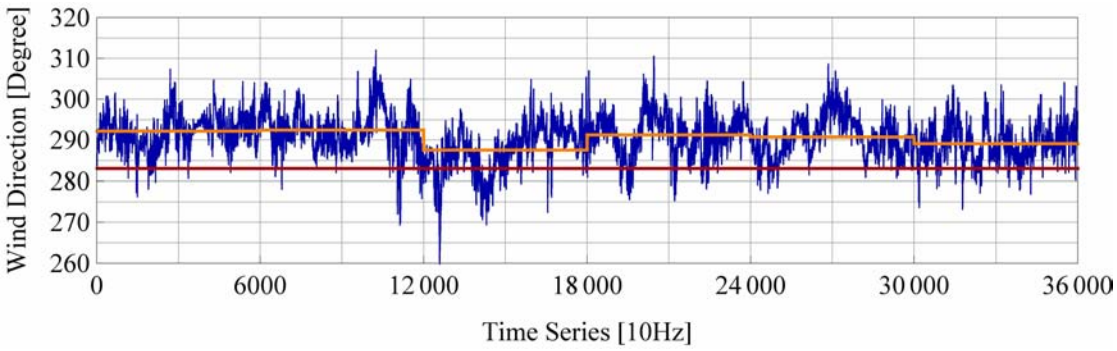

Figure 31: Time series (10 Hz) of the wind direction as measured by a Metek sonic anemometer at 32 m, during the period 12:20 - 13:20, on the 2009-05-05. The 10-min block averaged values are presented with orange and the yaw of the wind turbine with red.

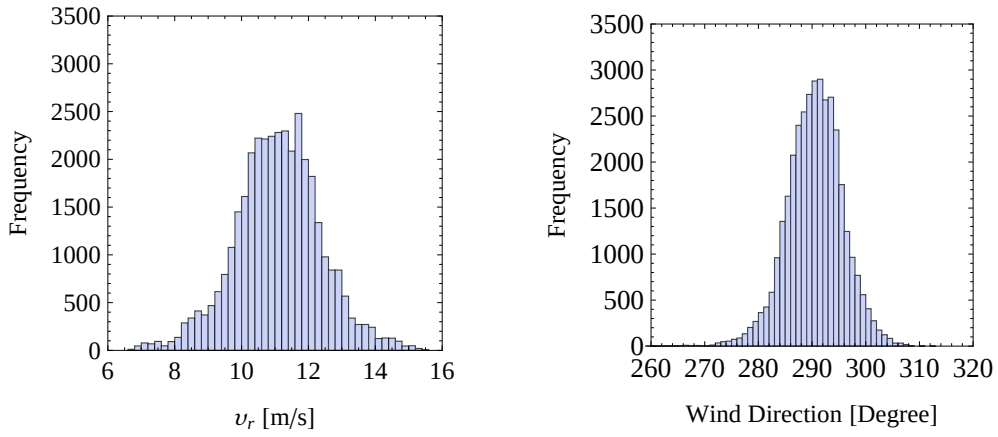

Figure 32: Frequency histograms of the radial wind speed (a) and of the wind direction (b) as measured by a lidar and a sonic, respectively.

B.2 Period B (2009-05-05 13:30 - 14:30)

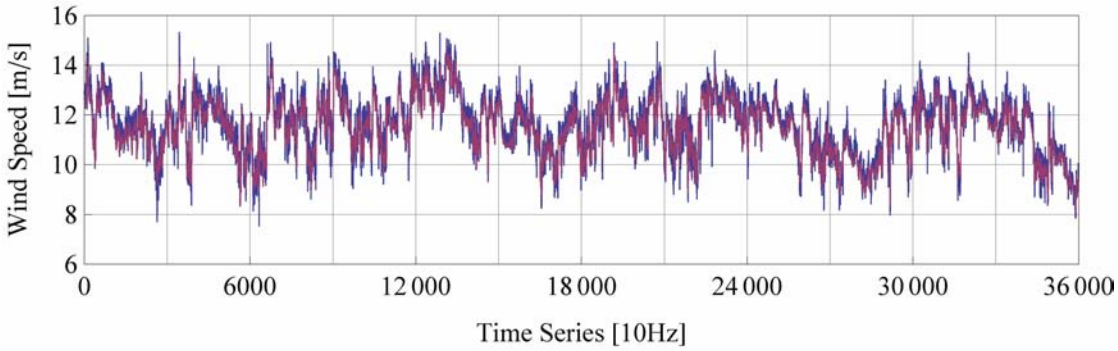

Figure 33: Time series (10 Hz) of the wind speed as measured by the ZephIR lidar (purple line) and by the Metek sonic anemometer (blue line), during the period 13:30 - 14:30, on the 2009-05-05.

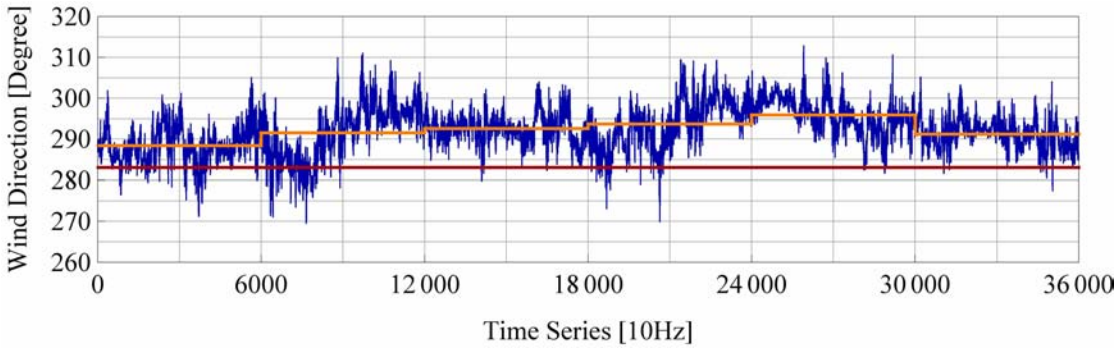

Figure 34: Time series (10 Hz) of the wind direction as measured by a Metek sonic anemometer at 32 m, during the period 13:30 - 14:30, on the 2009-05-05. The 10-min block averaged values are presented with orange and the yaw of the wind turbine with red.

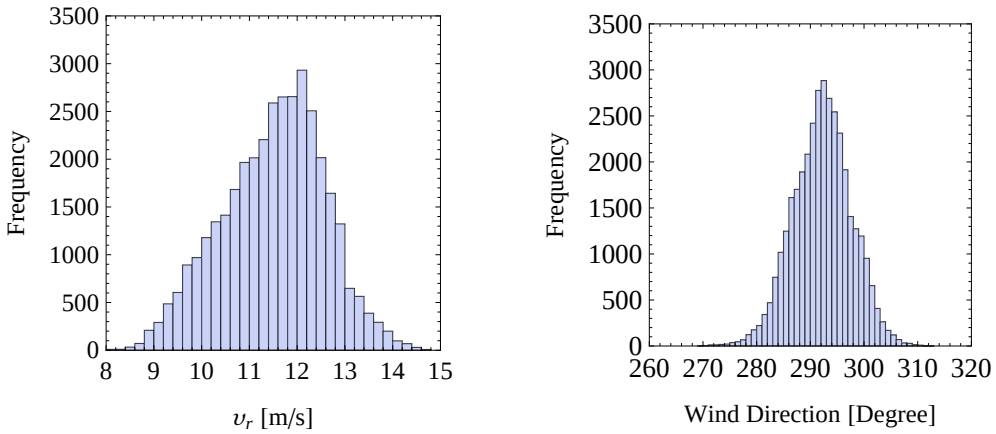

Figure 35: Frequency histograms of the radial wind speed (a) and of the wind direction (b) as measured by a lidar and a sonic, respectively.

B.3 Period C (2009-05-05 16:40 - 17:40)

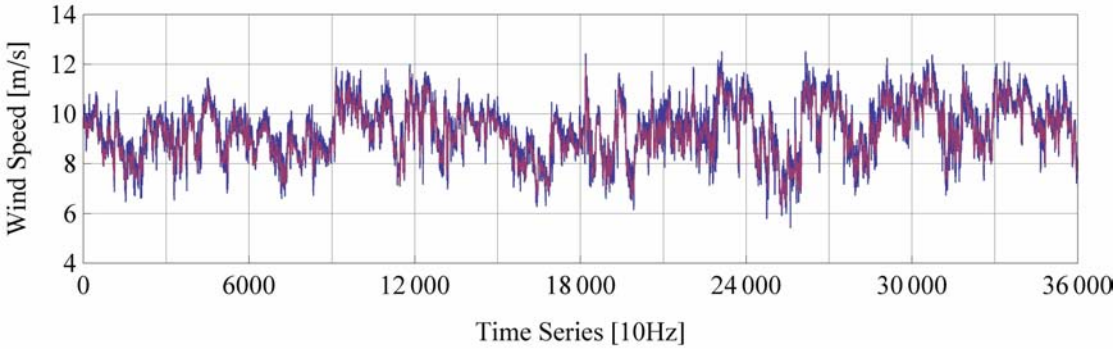

Figure 36: Time series (10 Hz) of the radial wind speed as measured by the ZephIR lidar during the period 16:40 - 17:40, on the 2009-05-05.

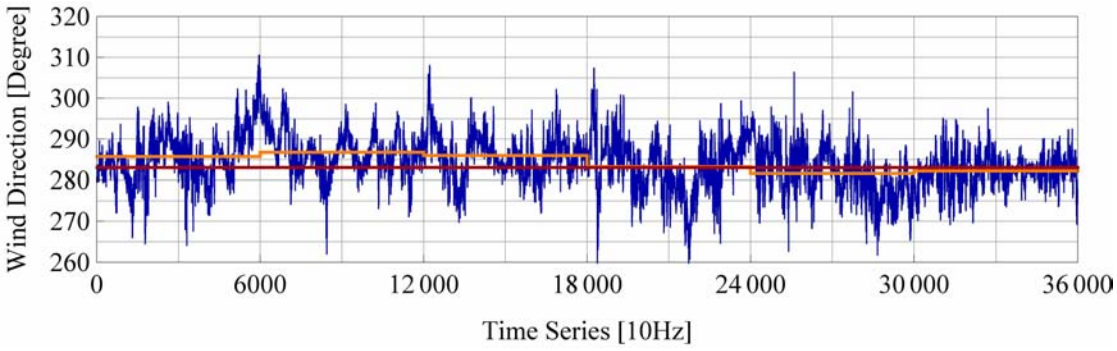

Figure 37: Time series (10 Hz) of the wind direction as measured by a Metek sonic anemometer at 32 m, during the period 16:40 - 17:40, on the 2009-05-05. The 10-min block averaged values are presented with orange and the yaw of the wind turbine with red.

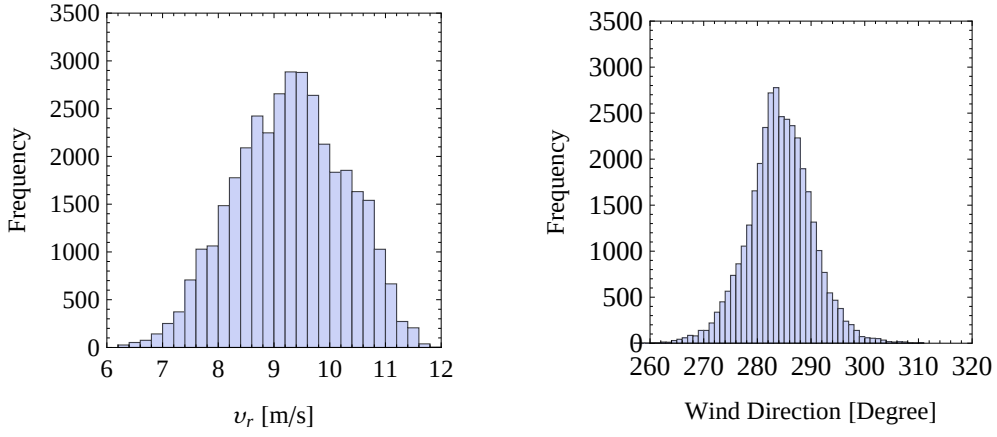

Figure 38: Frequency histograms of the radial wind speed (a) and of the wind direction (b) as measured by a lidar and a sonic, respectively.

B.4 Period D (2009-05-05 18:40 - 19:40)

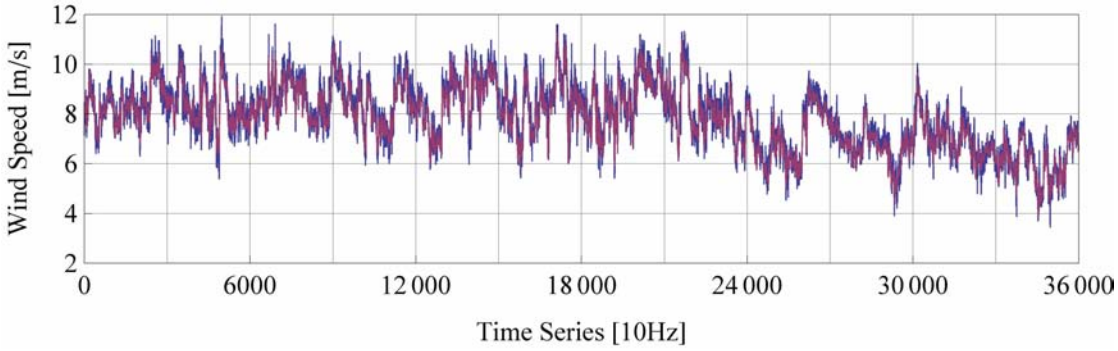

Figure 39: Time series (10 Hz) of the radial wind speed as measured by the ZephIR lidar during the period 18:40 - 19:40, on the 2009-05-05.

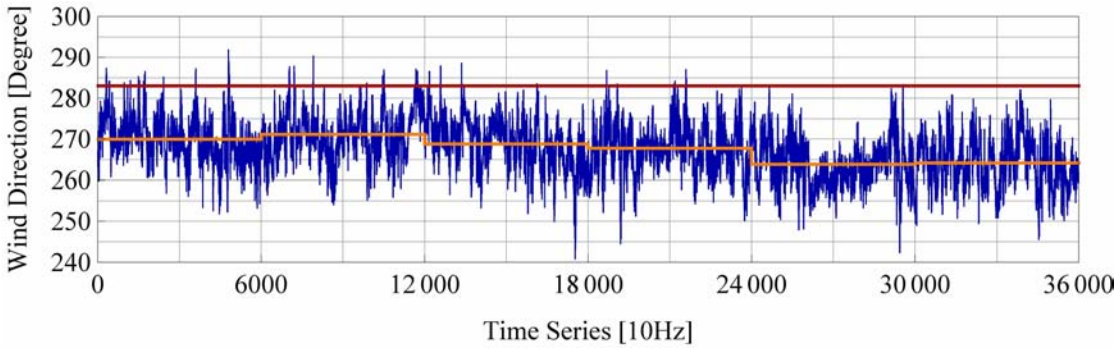

Figure 40: Time series (10 Hz) of the wind direction as measured by a Metek sonic anemometer at 32 m, during the period 18:40 - 19:40, on the 2009-05-05. The 10-min block averaged values are presented with orange and the yaw of the wind turbine with red.

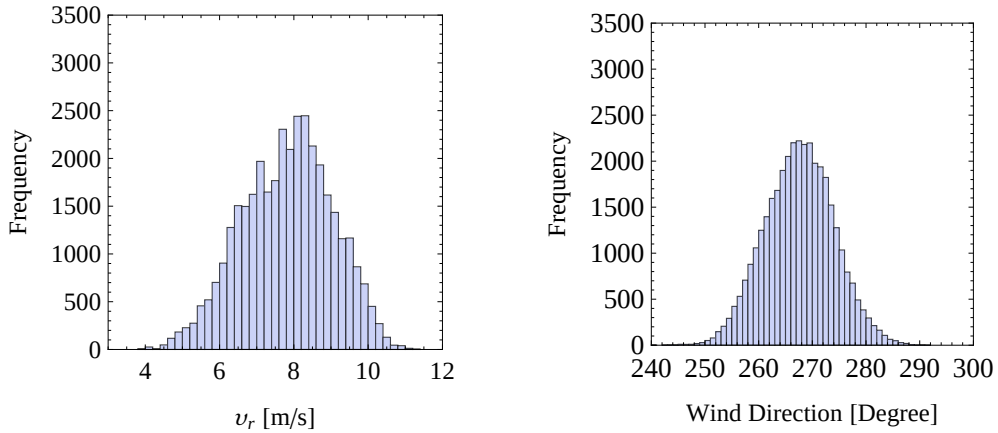

Figure 41: Frequency histograms of the radial wind speed (a) and of the wind direction (b) as measured by a lidar and a sonic, respectively.

C Correlation diagrams between lidar and sonic wind speed measurements

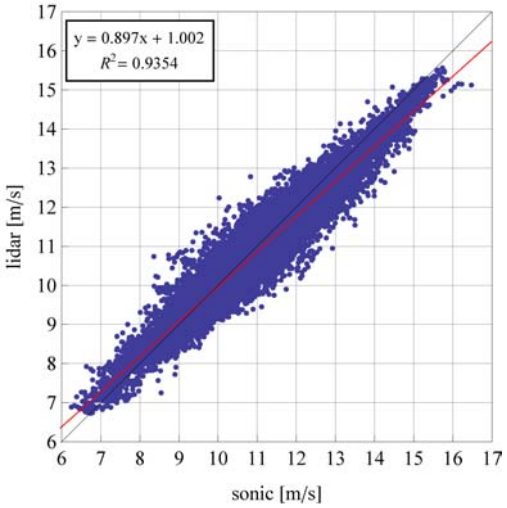

(a) 12:20 - 13:20

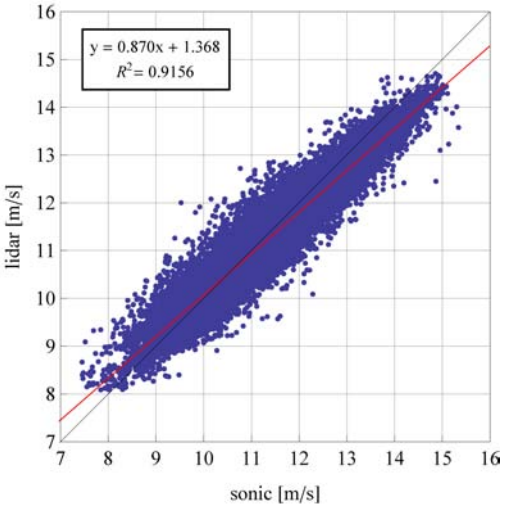

(b) 13:30 - 14:20

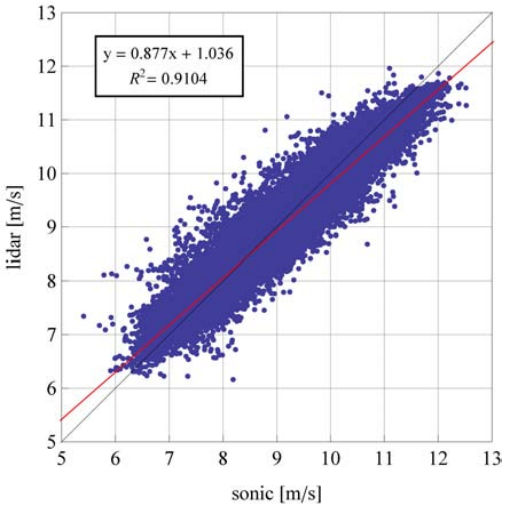

(c) 16:40 - 17:30

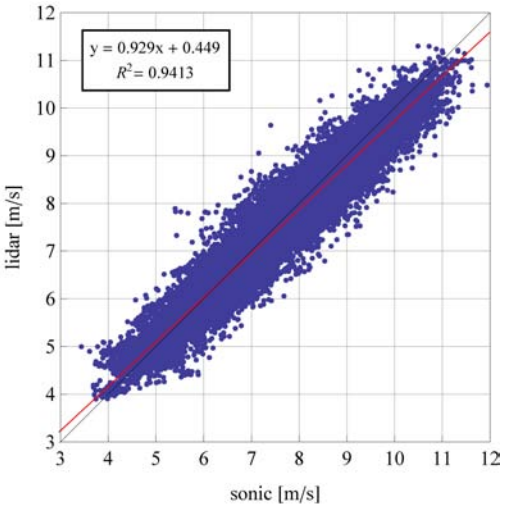

(d) 18:40 - 19:30

Figure 42: Correlation diagrams between lidar - sonic measurements.

D Spectral transfer function calculation

The theoretical spectral transfer function can be extracted through the frequency spectrum of the wind speed time series measured by the lidar and the sonic anemometer. According to the equation (8), the frequency spectrum (S_{v_r}) of the radial wind speed (v_r) is equal to:

$$S_{v_r}(f) = \int_{-\infty}^{+\infty} R_{v_r}(x_1)\, e^{-2\pi i x_1 f} dx_1 \tag{22}$$

Here $R_{v_r}(x_1)$ is the covariance between two wind speed values separated with a distance of x_1, which is calculated as:

$$\begin{aligned}
R_{v_r}(x_1) &= \langle v_r(x) \cdot v_r(x + x_1 e_1) \rangle \overset{(5)}{=} \\
&= \left\langle \int_{-\infty}^{+\infty} \varphi(s)\, n \cdot u(sn + x)\, ds \int_{-\infty}^{+\infty} \varphi(s')\, n \cdot u(s'n + x + x_1 e_1)\, ds' \right\rangle = \\
&= \left\langle \int_{-\infty}^{+\infty} \int_{-\infty}^{+\infty} \varphi(s)\, n \cdot u(sn + x)\, \varphi(s')\, n \cdot u(s'n + x + x_1 e_1)\, dsds' \right\rangle = \\
&= \int_{-\infty}^{+\infty} \int_{-\infty}^{+\infty} \varphi(s)\, \varphi(s')\, nn \langle u(sn + x) \cdot u(s'n + x + x_1 e_1) \rangle\, dsds' = \\
&= \int_{-\infty}^{+\infty} \int_{-\infty}^{+\infty} \varphi(s)\, \varphi(s')\, R_u((s' - s)\, n + x_1 e_1)\, dsds'
\end{aligned} \tag{23}$$

The $R_u((s' - s)\, n + x_1 e_1)$ corresponds to the covariance of the horizontal wind speed time series, which in this study is measured by a Metek sonic anemometer. Therefore

$$\begin{aligned}
S_u(f) &= \int_{-\infty}^{+\infty} R_u((s' - s)\, n + x_1 e_1)\, e^{-2\pi i f((s'-s)n + x_1 e_1)} dx_1 \\
&\Rightarrow \quad R_u((s' - s)\, n + x_1 e_1) = \int_{-\infty}^{+\infty} S_u(f)\, e^{2\pi i f((s'-s)n + x_1 e_1)} df
\end{aligned} \tag{24}$$

Using the equations (23) and (24) the frequency spectrum is given:

$$\begin{aligned}
S_{v_r}(f) &= \int_{-\infty}^{+\infty} R_{v_r}(x_1)\, e^{-2\pi i x_1 f} dx_1 \overset{(23)}{=} \\
&= \int_{-\infty}^{+\infty} \int_{-\infty}^{+\infty} \int_{-\infty}^{+\infty} \varphi(s)\, \varphi(s')\, R_u((s' - s)\, n + x_1 e_1)\, dsds' e^{-2\pi i x_1 f} dx_1 \overset{(24)}{=} \\
&= \int_{-\infty}^{+\infty} \int_{-\infty}^{+\infty} \int_{-\infty}^{+\infty} \varphi(s)\, \varphi(s') \times \\
&\qquad \times \int_{-\infty}^{+\infty} S_u(f')\, e^{2\pi i f'((s'-s)n + x_1 e_1)} df' dsds' e^{-2\pi i x_1 f} dx_1 =
\end{aligned}$$

$$
\begin{aligned}
&= \int_{-\infty}^{+\infty} \underbrace{\int_{-\infty}^{+\infty} \varphi(s)\, e^{-2\pi i f s n} ds}_{\hat{\varphi}^*(f')} \underbrace{\int_{-\infty}^{+\infty} \varphi(s')\, e^{2\pi i f s n} ds'}_{\hat{\varphi}(f')} \times \\
&\qquad \times \int_{-\infty}^{+\infty} S_u(f')\, e^{2\pi i f' x_1 e_1} e^{-2\pi i x_1 f} df' dx_1 = \\
&= \int_{-\infty}^{+\infty} \hat{\varphi}^*(f')\, \hat{\varphi}(f') \int_{-\infty}^{+\infty} S_u(f')\, e^{2\pi i f x_1 e_1} df' e^{-2\pi i x_1 f} dx_1 = \\
&= \int_{-\infty}^{+\infty} \hat{\varphi}^*(f')\, \hat{\varphi}(f')\, R_u(x_1)\, e^{-2\pi i x_1 f} dx_1 = \\
&= \left|\hat{\varphi}^*(f')\right|^2 S_v(f') \qquad (25)
\end{aligned}
$$

From the equation (25) it can be observed that the ratio of the spectra of the lidar and the sonic anemometer is equal with the square of the Fourier transform of the spatial weighting function ($\left|\hat{\varphi}^*(f')\right|$).

$$
\frac{S_{v_r}(f)}{S_u(f)} = \left|\hat{\varphi}^*(f')\right|^2 \qquad (26)
$$

Risø DTU is the National Laboratory for Sustainable Energy. Our research focuses on development of energy technologies and systems with minimal effect on climate, and contributes to innovation, education and policy. Risø has large experimental facilities and interdisciplinary research environments, and includes the national centre for nuclear technologies.

Risø DTU
National Laboratory for Sustainable Energy
Technical University of Denmark

Frederiksborgvej 399
PO Box 49
DK-4000 Roskilde
Denmark
Phone +45 4677 4677
Fax +45 4677 5688

www.risoe.dtu.dk